International Journal of Thermal Sciences 227 (2026) 110889

Contents lists available at ScienceDirect

International Journal of Thermal Sciences

journal homepage: www.elsevier.com/locate/ijts

Optimizing MNP injection for magnetic hyperthermia treatment: A three-dimensional study

Qian Jiang [a], Zhaokun Wang [a], Feng Ren [b], Chenglei Wang [c], Gholamreza Kefayati [d], Sasa Kenjeres [e], Kambiz Vafai [f], Xinguang Cui [g], Yang Liu [a], Hui Tang [a,*]

[a] Department of Mechanical Engineering, The Hong Kong Polytechnic University, Hong Kong, China
[b] School of Marine Science and Technology, Northwestern Polytechnical University, Xi'an, Shaanxi 710072, China
[c] Institute of High Performance Computing (IHPC), Agency for Science, Technology and Research (A*STAR), 1 Fusionopolis Way, #16-16 Connexis, Singapore 138632, Singapore
[d] School of Engineering, University of Tasmania, Hobart 7001, Tasmania, Australia
[e] Delft University of Technology, Faculty of Applied Sciences, Department of Chemical Engineering and J. M. Burgerscentrum Research School for Fluid Mechanics, Van der Maasweg 9, 2629 HZ Delft, The Netherlands
[f] Mechanical Engineering Department, University of California, Riverside, CA 92521, USA
[g] School of Aerospace Engineering, Huazhong University of Science and Technology, Wuhan, Hubei 430073, China

ARTICLE INFO

Keywords:
Magnetic hyperthermia treatment
Bioheat transfer
Particle swarm optimization
Lattice Boltzmann method

ABSTRACT

This work investigates optimal magnetic nanoparticle (MNP) injection strategies in three-dimensional (3D) tumor models to enhance the magnetic hyperthermia efficacy. We consider three tumor models with increasing geometric complexities: a spherical tumor, a simple irregular tumor (two connected spheres of different sizes), and a complex irregular tumor (three connected spheres of varying sizes). Centrosymmetric MNP distributions are employed for the spherical model, whereas asymmetric distributions are applied for the irregular models. The rapid convergence of the optimization demonstrates the efficiency and effectiveness of this 3D optimization framework. For the spherical tumor model, multi-site injections significantly enhance therapeutic outcomes under a 20-min waiting limit, whereas a single-site injection with a 114.9-min waiting time achieves 100% tumor ablation without damaging adjacent healthy tissue. Two injection sites suffice for the simple irregular tumor model, while a three-site strategy is optimal for the complex irregular model, indicating a relationship between required injection number and tumor geometry. Furthermore, the optimal MNP injection strategies correlate positively with the locations and sizes of the connected spheres. These findings produce more practical optimal strategies and provide broader, clinically relevant guidance for magnetic hyperthermia treatment.

1. Introduction

Magnetic hyperthermia is a localized thermal cancer therapy that can ablate tumor cells while sparing adjacent healthy tissue [1–4]. This characteristic effectively mitigates many side effects induced by traditional cancer treatments, and the efficacy of magnetic hyperthermia has been demonstrated in a range of clinical studies [5–7]. Heating is produced when injected magnetic nanoparticles (MNPs) are exposed to an external high-frequency alternating magnetic field (AMF), raising tumor temperature to approximately 43°C or higher and thereby inducing cell membrane damage and protein denaturation [8–11]. These mechanisms underscore the critical role of MNP properties and their distribution in determining treatment efficacy.

Iron oxide, particularly magnetite (Fe_3O_4), is the most commonly used MNP material in magnetic hyperthermia owing to its low toxicity and favorable biocompatibility [12–14]. However, excessive iron accumulation is not readily cleared by the human body, which may pose genotoxic risks to healthy skin and lung tissue and potentially reduce life expectancy [15,16]. In therapeutic applications, the particle sizes typically reported for magnetite yield superparamagnetic behavior, thereby establishing relaxation losses as the dominant heating mechanism, primarily via Néel and Brownian relaxation processes [17–22]. Néel relaxation corresponds to the reorientation of the magnetic moment within the crystal lattice of the particle, while Brownian relaxation arises from the physical rotation of the entire particle in the supporting medium. The heat generated by these mechanisms is commonly estimated using Rosensweig's model, which accounts for

* Corresponding author.
E-mail address: h.tang@polyu.edu.hk (H. Tang).

https://doi.org/10.1016/j.ijthermalsci.2026.110889
Received 9 January 2026; Received in revised form 26 March 2026; Accepted 31 March 2026
Available online 2 April 2026

Nomenclature

Abbreviations

AMF	Alternating magnetic field
CT	Computerized tomography
LBM	Lattice Boltzmann method
MNP	Magnetic nanoparticle
PBHTE	Pennes's bio-beat transfer equation
PSO	Particle swarm optimization

Greek Letters

α	Thermal diffusivity, m^2/s
χ_0	Equilibrium susceptibility
μ_0	Vacuum permeability, Tm/A
ω	Weighting factors of requirement
Φ	Volume fraction with time variant
ϕ	Volume fraction without time variant
ϕ_0	Reference volume fraction
ρ	Density, kg/m^3
σ	Standard deviation, mm
σ_0	Reference standard deviation, mm
τ_R	Effective relaxation time, s

Roman Letters

(k_x, k_y, k_z)	Coordinate ratio
(x, y, z)	Cartesian coordinate, mm
(x_0, y_0, z_0)	Reference Cartesian coordinate, mm
$\dot{m}$	Mass flow rate, kg/m^3-s
c	Specific heat capacity, J/(kg-K)
D	Mass diffusivity, m^2/s
d	distance of injection site, mm
d_0	Reference distance, mm
f	Frequency of AMF, Hz
H_0	Intensity amplitude of AMF, A/m
J	Objection function
k	Thermal conductivity, W/m-K
k_ϕ	Volume fraction ratio
k_σ	Standard deviation ratio
k_d	Distance ratio of injection site
L	Length of healthy tissue block, mm
l	Length of cube for tumor dimensions, mm
Le	Lewis number
N	Number of sampled points at the interface
n	Number of injection sites
O	Sphere center
Q	Heat source density from MNPs, W/m^3
R_{dose}	Requirement of MNP dose
R_{hea}	Temperature requirement in healthy tissue
R_{int}	Temperature requirement at interface
R_{tum}	Temperature requirement in tumor tissue
S	Injection site
T	Temperature, ° C
t	Time, min
V	Volume, mm^3

Subscripts

A	Amplitude
b	Blood
hea	Healthy tissue
i	Injection site index
max	Maximum value
nf	Nanofluid, the mixture of tissue and injected MNPs
opt	Optimal value
tum	Tumor tissue

both relaxation losses and is influenced by the local volume fraction of MNPs [23].

An appropriate distribution of MNPs should generate sufficient heat to ablate tumor tissue while minimizing damage to surrounding healthy tissue [24]. A relatively uniform MNP distribution is preferred generally because it yields a milder thermal profile and is often modeled as a Gaussian distribution with a large standard deviation [4,25]. Gaussian concentration profiles naturally arise from diffusion and are supported by theoretical analyses and experimental observations [26,27]. Accordingly, diffusion-derived MNP distributions are frequently combined with multi-site injection strategies to enlarge the heated region and produce a gentler temperature profile that reduces the risk of overheating and inflammation [24,28–30].

To achieve optimal MNP distribution and maximize treatment efficacy, particularly for irregular tumor geometries, an optimization algorithm integrated with the widely used Pennes bioheat transfer equation (PBHTE) [31] provides an effective approach. While local optimization algorithms (e.g., the Nelder–Mead simplex method and the epsilon-constraint approach) are predominantly applied to this problem, they suffer from significant limitations, primarily their sensitivity to initial parameter assumptions [32–34]. As a result, these methods can produce suboptimal distributions constrained by the algorithmic limitations [35]. Additionally, although global optimization algorithms can remove over 90% of the tumor region in many simulations, earlier studies have not obtained completely satisfactory outcomes, possibly owing to suboptimal settings or algorithmic defects, resulting in visibly incomplete tumor ablation or unintended damage of healthy tissue [36,37]. Comparatively, particle swarm optimization (PSO) demonstrates improved performance due to its reduced dependence on initial conditions and its broader search space [36]. Recent studies by Jiang et al. [38,39] applied PSO to identify MNP injection strategies that ablate all tumor cells while preserving surrounding healthy tissue, demonstrating the effectiveness of PSO for optimizing MNP distributions in magnetic hyperthermia. However, these studies are restricted to two-dimensional (2D) configurations and, despite some reporting excellent optimization outcomes, may not capture the geometric and transport complexities of realistic three-dimensional (3D) treatment environments, particularly for irregular tumor shapes. To date, studies addressing MNP distribution optimization in fully 3D configurations remain limited [32,40], underscoring the need for dedicated 3D injection-optimization research to better approximate clinical conditions.

To bridge this gap, a 3D simulation framework is developed based on PBTHE, which incorporates the PSO algorithm to determine the optimal spatial distribution of MNPs and maximize treatment efficacy. To ensure the simulations closely approximate realistic 3D tumor geometries, various irregularities in tumor geometries are considered by employing combinations of different spheres. Despite its simple elements, the developed tumor model can theoretically represent any possible shape. Both single-site and multi-site injections are considered in our investigation to facilitate optimal 3D strategies. Additionally, the independent parameter search is incorporated into the MNP injection optimization to accommodate the irregular geometries. The effects of the MNP injection number and waiting-time constraint are examined. Furthermore, we explore geometry-dependent injections to provide a general guideline for optimal strategies.

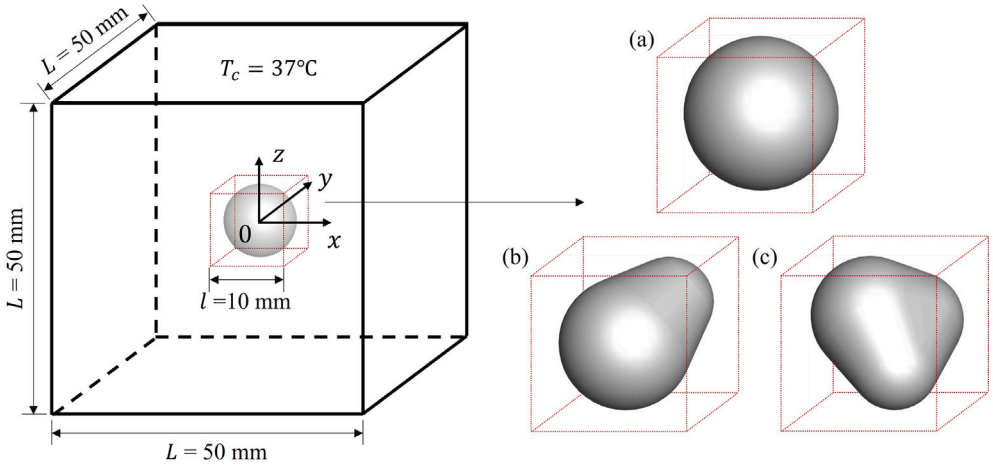

Fig. 1. Schematics of three tumor models embedded within a healthy tissue block. (a) the spherical tumor model, (b) the simple irregular tumor model, and (c) the complex irregular tumor model. The gray surface denotes the tumor boundary, while the red dashed cube defines the size of the tumors.

The remainder of this paper is organized as follows: Section 2 presents the physical and mathematical problems, along with the optimization model utilized in this work. Section 3 details the results categorized by tumor model, including the spherical tumor model in Section 3.1, the simple irregular tumor model in Section 3.2, the complex irregular tumor model in Section 3.3, and a general discussion of geometry-dependent injection strategies in Section 3.4. Finally, Section 4 summarizes the key findings.

2. Problem description and methodology

This section introduces the physical problem and the mathematical methods employed in the present work. The problem description is given in Section 2.1, followed by the governing equations in Section 2.2. The optimization settings are described in Section 2.3.

2.1. Problem description

As illustrated in Fig. 1, a spherical tumor and two irregular tumors embedded at the center of the healthy tissue block are considered in this study. The simple irregular tumor consists of two connected spheres of different sizes, while the complex irregular tumor comprises three connected spheres of different sizes. All three models are contained in a red cube with a side length of $l = 10$ mm (a dimension frequently observed in clinical contexts [41,42]) and are tangent to all six cubic faces. Although these three models remain simplified compared to realistic tumors, they represent a way of introducing geometric complexity. Accordingly, they are adopted to demonstrate the performance of the current simulation framework and, more importantly, to derive general guidelines for MNP optimization. To facilitate analysis, a Cartesian coordinate system is defined, with the origin located at the center of the red cube. In the simple irregular tumor model, the centers of the two spheres are randomly designated at $O_1(-0.5, -0.5, -0.5)$ mm and $O_2(2,2,2)$ mm, with the radii of 4.5 mm and 3 mm, respectively. In the complex irregular tumor model, the centers of the three spheres are $O_1(-1,0,1)$ mm, $O_2(1, -2, -2)$ mm, and $O_3(2.25,2.25,0.5)$ mm, with radii of 4 mm, 3 mm, and 2.75 mm, respectively. The side length of the tissue block is $L = 50$ mm, which is sufficiently large to ensure negligible influence from the outer boundaries, as verified in Appendix A. Continuity of temperature and of the normal heat flux is enforced at the interface between the tumor and the surrounding healthy tissue. The initial temperature is set as a constant $T_c = 37°C$ to represent the normal temperature of the human body, and this value is upheld at the outer boundaries throughout the simulation.

2.2. Governing equations

The temperature T in both the tumor and healthy tissue is governed by the 3D PBHTE, as

$$(\rho c)_{nf}\frac{\partial T}{\partial t} = k_{nf}\left(\frac{\partial^2 T}{\partial x^2} + \frac{\partial^2 T}{\partial y^2} + \frac{\partial^2 T}{\partial z^2}\right) + \dot{m}_b c_b (T_b - T) + Q, \tag{1}$$

where ρ, c, and k denote the density, specific heat capacity, and thermal conductivity, respectively. The subscript "b" specifies the properties of blood, while "nf" represents the modified tissue, which can be regarded as a nanofluid composed of the original tissue (tumor and healthy tissue) and the embedded MNPs. The thermal properties of nanofluids are influenced by the volume fraction ϕ of MNP in the tissue [43–45], and the relevant equations along with their respective properties can be found in our previous work [38].

The term $\dot{m}_b c_b (T_b - T)$ in Eq. (1) denotes the heat sink induced by blood perfusion, where $\dot{m}_b$ represents the perfusion mass flow rate. In practice, $\dot{m}_b$ is temperature-dependent and differs between healthy and tumor tissues [46]. The term Q refers to the heat source released from MNPs when exposed to an external AMF. In this work, Q is evaluated using Rosensweig's model owing to the superparamagnetic property of MNPs utilized and their low propensity for chain formation [17,18,47]. The Rosensweig's model is given by [23]

$$Q = \pi \mu_0 \chi_0 \phi H_0^2 f \frac{2\pi f \tau_R}{1 + (2\pi f \tau_R)^2}, \tag{2}$$

where H_0 and f denote the amplitude and frequency of the external AMF. In the present work, we assume a spatially uniform AMF across the tissue block because the investigated tissue volume is extremely small compared to the spatial variation scale of the AMF [48]. The field parameters used are $H_0 = 8\times10^3$ A/m^2 and $f = 4\times10^5$ Hz [49]. μ_0, χ_0, and τ_R represent the vacuum permeability, equilibrium susceptibility, and effective relaxation time, respectively. Detailed values and calculations for these parameters can be found in our previous work [38]. ϕ denotes the local volume fraction of the MNP.

The distribution of MNP can be analytically determined by the diffusion equation [26]. Consequently, the volume fraction at a given site (x, y, z) and a specific time t caused by the ith injection is obtained by

$$\Phi_i(x, y, z, t) = \frac{V_i}{(4\pi D t_i)^{3/2}} \exp\left[-\frac{(x - x_i)^2 + (y - y_i)^2 + (z - z_i)^2}{4 D t_i}\right], \tag{3}$$

where (x_i, y_i, z_i) denotes the coordinates and V_i represents the MNP volume of the ith injection. The parameter D specifies the diffusivity of MNP in tissue. Eq. (3) describes the 3D Gaussian distribution of the MNP at time t, with the variance $2Dt$, which arises from a period

of MNP diffusion before the application of the AMF. Given the large value of the Lewis number, $Le = \alpha/D = 125$ (where α denotes the thermal diffusivity), MNP distribution during the treatment (after AMF application) can be assumed to be time-frozen [50]. Therefore, for a given waiting time before AMF application, the MNP distribution resulting from ith injection can be re-expressed as

$$\phi_i(x,y,z) = \frac{V_i}{(2\pi\sigma_i^2)^{3/2}} \exp\left[-\frac{(x-x_i)^2+(y-y_i)^2+(z-z_i)^2}{2\sigma_i^2}\right], \tag{4}$$

where $\sigma_i^2 = 2Dt_i$. For multi-site injections, the total volume fraction at location (x, y, z) is obtained through superposition of the contributions from each injection [34,51], as

$$\phi(x,y,z) = \sum_{i=1}^{n} \phi_i(x,y,z), \tag{5}$$

where n denotes the number of injections.

Eq. (1) is solved using the D3Q7 MRT-LBM scheme throughout the domain, which ensures the temperature condition at the interface of the tumor and healthy tissue. A detailed introduction to this scheme, along with its validation is provided in Appendix A.

2.3. Optimization

The optimization in this work aims to identify the optimal MNP distribution that maximizes treatment efficacy, with the resulting temperature distribution serving as the primary performance metric [32,36,51]. For each injection, the three spatial coordinates (x_i, y_i, z_i), the waiting time t_i before AMF application, and the MNP injection dose V_i constitute five key physical variables. To facilitate the optimization search, we use five derived parameters: the injection location (x_i, y_i, z_i), the standard deviation of MNP distribution σ_i (related to t_i), and the peak volume fraction amplitude ϕ_{Ai} (dependent on both V_i and σ_i). These parameters are normalized to the range [0,1] for comparison during the optimization, as: $k_{\sigma,i} = \sigma_i/\sigma_0$, $k_{\phi,i} = \phi_{Ai}/\phi_0$, and $(k_{x,i}, k_{y,i}, k_{z,i}) = (x_i/2x_0 + 0.5, y_i/2y_0 + 0.5, z_i/2z_0 + 0.5)$, where σ_0, ϕ_0, and (x_0, y_0, z_0) are the chosen reference values. Specifically, σ_0 is derived from the limits of the maximum allowed waiting time before AMF application, while the three reference coordinates (x_0, y_0, z_0) are assumed to be identical in this work. In the spherical tumor model, each injection shares the same ϕ_A and σ for simplification due to the centrosymmetric characteristics of the model. Injection locations are searched in centrosymmetric constraint based on their distance d from the tumor center (the coordinate origin). Distance is normalized as $k_d = d/d_0$, where d_0 is the reference distance and k_d the corresponding normalized ratio. Note that the subscript "i" is omitted in the spherical tumor model due to the identical parameters of each injection. Using these parameters and ratios, Eq. (4) can be rewritten as

$$\phi_i(x,y,z) = k_{\phi,i}\phi_0 \exp\left[-\frac{(x-x_i)^2+(y-y_i)^2+(z-z_i)^2}{2k_{\sigma,i}^2\sigma_0^2}\right], \tag{6}$$

Therefore, the physical variables can be obtained by

$$t_i = \frac{k_{\sigma,i}^2\sigma_0^2}{2D}, \tag{7a}$$

$$V_i = (2\pi)^{3/2}\phi_0 k_{\phi,i}\sigma_0^3 k_{\sigma,i}^3, \tag{7b}$$

$$(x_i, y_i, z_i) = \left(2(k_{x,i}-0.5)x_0, 2(k_{y,i}-0.5)y_0, 2(k_{z,i}-0.5)z_0\right). \tag{7c}$$

Specifically, for the spherical tumor case the distance is given by

$$d = k_d d_0 \tag{8}$$

To obtain the optimal combination of these variables, we define a set of optimization criteria that emphasize the temperature distribution while accounting for MNP dose, thereby seeking the best overall treatment performance. Two critical temperature thresholds are considered: 43°C, the threshold for cell ablation [32], and 46°C, the upper limit chosen to avoid inflammatory response [30]. Consequently, to achieve optimal treatment efficacy, i.e., complete ablation of tumor tissue with preservation of surrounding healthy tissue using a minimal MNP dose, we define four performance indicators as

$$R_{tum} = \frac{V_{43\le T<46°C \text{ in tumor}}}{V_{\text{tumor}}}, \tag{9a}$$

$$R_{hea} = \frac{V_{T<43°C \text{ in healthy tissue}}}{V_{\text{healthy tissue}}}, \tag{9b}$$

$$R_{int} = \exp\left(-\sqrt{\frac{1}{N}\sum_{i=1}^{N}(T_i - 43)^2}\right), \tag{9c}$$

$$R_{dose} = 1 - \sqrt[4]{\sum_{i=1}^{n} k_{\phi,i}k_{\sigma,i}^3}, \tag{9d}$$

where V and N denote the volume and the number of sampled points on the tumor boundary, respectively. R_{tum} defines the volume ratio of the tumor where temperatures lie between 43°C and 46°C, while R_{hea} denotes the volume ratio of the healthy tissue where temperatures remain below 43°C. R_{int} specifies the degree of agreement between the 43°C isotherm and the tumor boundary. R_{dose} represents the MNP dose, since the dose of each injection is proportional to $k_{\phi,i}k_{\sigma,i}^3$, as shown in Eq. (7b). The theoretical maximum value for each indicator is 1, indicating complete satisfaction of the corresponding criterion. This ideal is achieved only when the entire tumor is lies within 43°C–46°C, surrounding healthy tissue remains below 43°C, and the tumor–healthy interface coincides with the 43°C isotherm, accomplished without MNP intake. The combination of the these four requirements defines the objective function J for optimization, which is formulated as

$$J = \omega_1 R_{tum} + \omega_2 R_{hea} + \omega_3 R_{int} + \omega_4 R_{dose}, \tag{10}$$

where $\omega_1 \sim \omega_4$ represent the weighting factors for the four indicators, assigned values of 0.5, 0.3, 0.1, and 0.1, respectively. These weights were selected empirically through preliminary trials to balance the contributions of the individual indicators, and to scale the objective function J approximately vary within the range [0,1].

The objective function J is maximized using the PSO algorithm. The PSO methodology is described in detail in Appendix B, and its convergence and performance on multimodal problems have been well validated in our previous work [38]. The optimal parameter set generated from the optimization is converted back into the corresponding optimal physical variables via Eqs. (7) and (8), thereby providing actionable guidance for practical treatment applications. Obtaining the global optimum requires evaluating a large number of candidates within a single optimization run, which results in a time-consuming simulation. Therefore, taking advantage of the suitability of the LBM for GPU acceleration [52], we implement the simulations on NVIDIA GeForce RTX 3090 GPUs to improve computational efficiency. With this implementation, a single optimization run comprising 300 generations with 20 particles per generation requires roughly six days of wall-clock time on the specified hardware.

3. Results and discussions

The discussions are organized according to the three representative tumor models: a spherical tumor model (centrosymmetric) in Section 3.1, a simple irregular tumor model (axisymmetric) in Section 3.2, and a complex irregular tumor model (general) in Section 3.3. Based on the optimal outcomes for these three tumor geometries, geometry-dependent injection strategies are discussed in Section 3.4.

3.1. Spherical tumor

3.1.1. Effect of injection number

The centrosymmetry of the spherical tumor model permits injections that are symmetrically arranged about the tumor center and that share identical Gaussian distribution. The reference distance is set to $d_0 = 4.5$ mm (90% of the tumor radius). The reference volume fraction is $\phi_0 = 0.05$ to ensure the applicability of the employed nanofluid model [38,43]. The reference Gaussian standard deviation for the baseline scenario is $\sigma_0 = 1.55$ mm, corresponding to the maximum allowed waiting time of 20 min. Accordingly, three normalized ratio k_ϕ, k_σ, and k_d are involved in the optimization search.

Four injection scenarios are considered in this section: one-, four-, six-, and eight-site injections. In the one-site scenario, the centrosymmetric configuration requires the injection to be placed at the tumor center, naturally resulting in $k_d = 0$. In the four-site scenario, one injection is located on the z-axis at $z = d$, while the other three are positioned equidistantly on the plane $z = -d/3$. The coordinates of the four injection sites are therefore: $(0, 0, d)$, $(0, 2\sqrt{2}d/3, -d/3)$, $(\sqrt{6}d/3, -\sqrt{2}d/3, -d/3)$, and $(-\sqrt{6}d/3, -\sqrt{2}d/3, -d/3)$. By analogy, the coordinates for the six-site scenario are $(\pm d, 0, 0)$, $(0, \pm d, 0)$, and $(0, 0, \pm d)$. For the eight-site scenario, the sites are located at $(\pm d/\sqrt{3}, \pm d/\sqrt{3}, \pm d/\sqrt{3})$, with all eight sign combinations.

The optimization was run for 300 generations with a swarm of 20 particles per generation. For demonstration, Figs. 2(a) and (b) depict the convergence behavior of the eight-site injection scenario, explicitly showing the evolution of each particle throughout the optimization. Initially, the normalized ratios (k_ϕ, k_σ, and k_d) are randomly scattered, resulting in 20 correspondingly random objective function values. Pronounced adjustments in the three ratios occur in the second generation, accompanied by a rapid increase in the maximum objective function from $J = 0.666$ to 0.806. After several further iterations, the normalized ratios converge toward their respective optimal values, and the objective function values increase steadily until the global maximum is attained, consistent with the typical search dynamics of PSO [53]. The final maximum objective value ($J = 0.891$) is achieved with the optimized normalized ratios ($k_\phi = 0.081$, $k_\sigma = 0.982$, and $k_d = 0.888$), representing the optimal solution for the eight-site injection scenario.

Figs. 2(c) to (f) show the evolution of the maximum objective function J and the corresponding normalized ratios k_ϕ, k_σ, and k_d, for the different injection numbers. The one-site injection scenario, owning to its smallest parameter space, converges most rapidly, with optimal results obtained within approximately 50 generations. The remaining scenarios, having larger parameter spaces, require more generations to converge, but nonetheless reach their optima within 150 generations, which reflects the effectiveness of the chosen optimization algorithm and problem setup. Generally, increasing the number of injections improves the converged optimal outcome, with the eight-site injection strategy achieving the best performance among the cases considered, consistent with trends reported for 2D configurations by Jiang et al. [38]. Notably, both k_ϕ and k_d decrease as the number of injections increases, whereas k_σ remains close to 1 in each scenario.

Fig. 3 illustrates the optimization trajectories of the objective function J plotted against treatment efficacy indicators (R_{tum} and R_{hea}) and MNP dose (V) for the different injection numbers. Over the full optimization (300 generations) plus 20 additional randomly generated initial candidates, a total of 6020 candidate solutions are evaluated during the PSO iterations, using a color scale ranging from dark green to red for visualization. Early generation points are broadly dispersed across the parameter space for each scenario and progressively migrate toward regions with higher J. The converged maximum objective value increases monotonously across the four injection scenarios, from $J = 0.714$ for the one-site injection to $J = 0.891$ for the eight-site injection (see Table 1), underscoring the superior performance of the eight-site configuration and corroborating the trends in Fig. 2.

Table 1
Optimal strategies for the one-site, four-site, six-site, and eight-site injection scenarios applied to the spherical tumor model.

Injection strategy	One-site	Four-site	Six-site	Eight-site
R_{tum}	0.602	0.916	0.988	1.000
R_{hea}	1.000	0.999	0.999	1.000
R_{int}	0.992	0.457	0.706	0.800
R_{dose}	0.140	0.098	0.107	0.116
J	0.714	0.813	0.875	0.891
T_{max}, °C	56.6	46.2	46.0	46.0
t_{opt}, min	19.9	20.0	20.0	19.3
V_{opt}, mm^3	1.60	1.94	1.86	1.79
d_{opt}, mm	–	4.35	4.08	4.00

As shown in Figs. 3 (a1) to (d1), the trajectories of R_{tum} versus J exhibit approximately linear trends in each scenario. Increases in R_{tum} produce substantial increases in J due to the strong positive contribution of R_{tum} to J. A similar relationship persists when the number of injection sites increases to four, and all four scenarios share a common intercept value. This intercept (=0.32) is primarily attributable to R_{hea}, which arises either when the temperature throughout the domain remains below 43°C (no damage to tumor or healthy tissue) or when tumor temperatures exceed 46°C (causing an inflammatory response). Variations in R_{int} and R_{dose} introduce scatter around this intercept. The slope (=0.56) is dominated by the contribution of R_{tum}, with minor coupling effects from the other indicators. Specifically, the one-site injection exhibits a different (lower) slope, which likely reflects substantial overheating (volumes exceeds 46°C) induced by the concentrated heat source, which impedes further increases in R_{tum}. Overall, increasing the number of injections elevates the optimal R_{tum}, and the eight-site injection attains the maximum possible value $R_{tum} = 1$. The optimal R_{hea} value shown in Figs. 3 (a2) to (d2) closely satisfy the prescribed requirement, indicating minimal difference in their contributions to the variation of the maximum J. Regarding the MNP dose V, the absence of MNP results in no temperature elevation and, consequently, no ablation, keeping all tissues below 43°C. Conversely, excessive dosing readily drives tumor temperatures above 46°C. Both extremes correspond to low objective values J, as illustrated in Figs. 3 (a3) to (d3). Even at the smallest optimal MNP doses among the four scenarios, the poor R_{tum} performance indicates that the one-site injection cannot achieve satisfactory results in J.

The details of the optimal injection strategies for the different injection number are summarized in Table 1, and the corresponding temperature fields and MNP injection sites are shown in Fig. 4. The pronounced overheating region (where the temperature exceeds 46°C) in the optimal one-site injection reduces R_{tum} to 0.602 (39.8% of the tumor volume overheated), which largely prevents this strategy from achieving a satisfactory outcome. Despite this limitation, the one-site injection strategy nearly meets the other requirements, including the performance in healthy tissue R_{tum}, interface R_{int}, and MNP dose R_{dose}, as detailed in Table 1. Both the four-site and six-site injection strategies are inferior in R_{int}, while the four-site strategy also exhibits a slight deficit in R_{tum}. Comparatively, high scores in R_{tum} and R_{int} drive the eight-site injection strategy to achieve the largest value in J among the four strategies. The maximum temperature decreases as the number of injections increases, reaching exactly 46°C for both the six-site and eight-site strategies. Additionally, the optimal injection sites tend to move toward the tumor center as the number of injections rises, as indicated by d_{opt} shown in Table 1, although the change is subtle yet visible in Figs. 4 (b1) to (d1). Notably, the optimal waiting time t_{opt} for all four injection strategies approaches the 20-minute upper bound, raising the question of how performance will change if the allowable waiting time is extended. Consequently, the impact of the waiting time constraint for the one-site and eight-site injection scenarios, the most promising and highest-performing cases, is analyzed below.

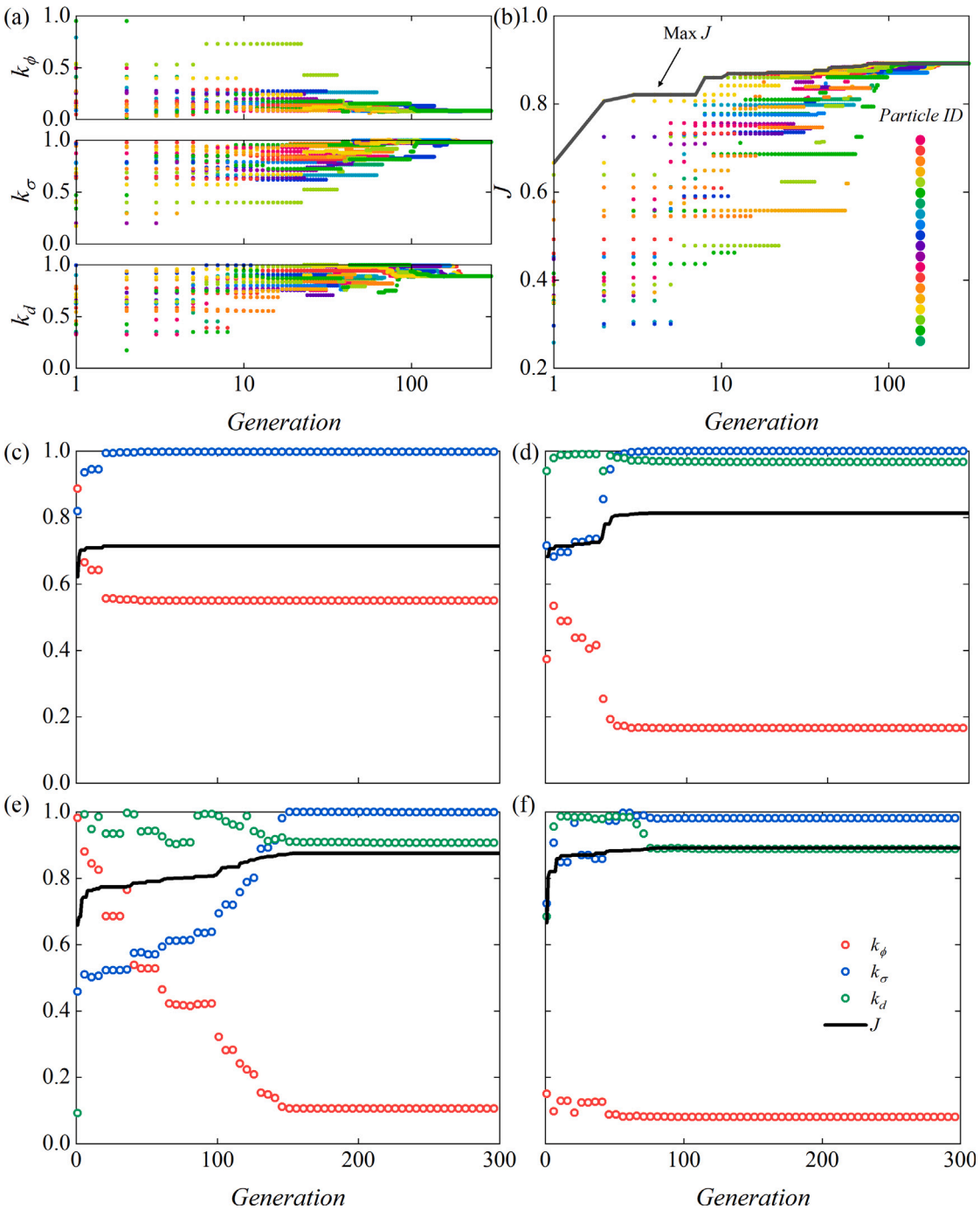

Fig. 2. PSO convergence process for the spherical tumor model: Evolution of (a) the three normalized ratios, i.e., k_ϕ, k_σ and k_d; (b) the objective function J for each particle in the eight-site injection scenario, where the black line denotes the envelope of the maximum J. Evolution of the maximum objective value J and their corresponding normalized ratios k_ϕ, k_σ, and k_d for the scenarios of (c) one-site injection, (d) four-site injection, (e) six-site injection, and (f) eight-site injection.

Table 2
Optimal strategies for the one-site injection scenario under different allowed waiting times for the spherical tumor model.

Time limit	R_{tum}	R_{hea}	R_{int}	T_{max}, °C	V_{opt}, mm^3	t_{opt}, min
20 min	0.602	1.000	0.992	56.6	1.60	19.9
60 min	0.851	1.000	0.996	48.4	1.76	59.2
120 min	1.000	1.000	0.997	46.0	2.19	114.9

3.1.2. Effect of maximum allowed waiting time

For the one-site injection scenario, two additional allowed waiting times (60 min and 120 min) are considered alongside the baseline 20-minute limit, yielding reference standard deviations σ_0 = 1.55, 2.68, and 3.80 mm, for the 20, 60, and 120-minute cases, respectively. The obtained optimal waiting times (t_{opt}) for these three scenarios are 19.9, 59.2, and 114.9 min, respectively. The corresponding optimal temperature fields (see Figs. 5(a) to (c)) indicate that the 114.9-minute wait is sufficient to eliminate the overheated region. As summarized in Table 2, the overheated tumor fraction is reduced from 39.8% (R_{tum} = 0.602) at t_{opt} = 19.9 min to 14.9% (R_{tum} = 0.851) at t_{opt} = 59.2

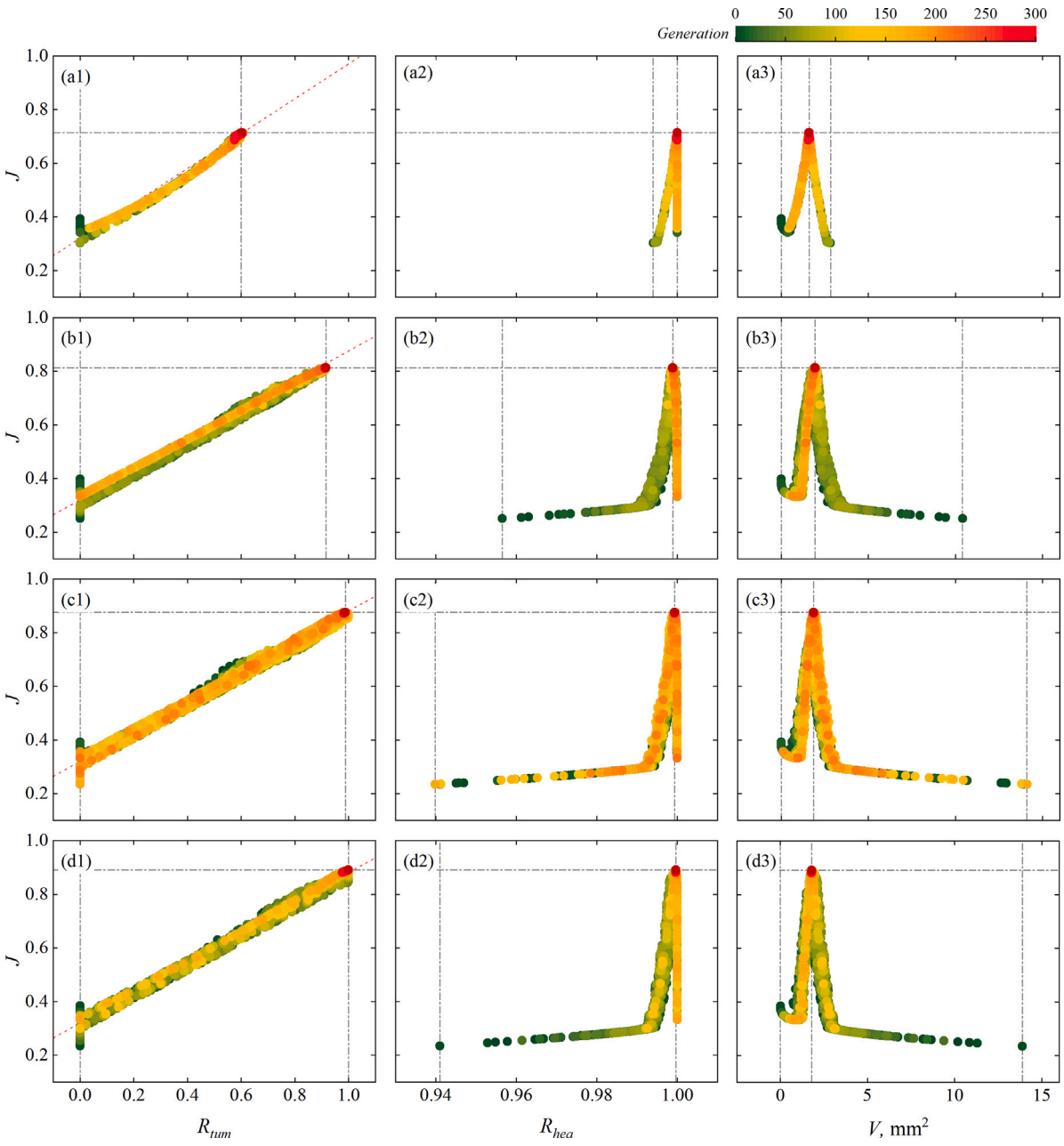

Fig. 3. Optimization trajectory for the spherical tumor model showing the satisfied tumor ratio R_{tum}, the satisfied healthy tissue ratio R_{hea}, and the required MNP dose V, for the scenarios: (a1)~(a3) one-site injection, (b1)~(b3) four-site injection, (c1)~(c3) six-site injection, and (d1)~(d3) eight-site injection. The dark red point denotes the optimal choice.

min, and vanishes entirely (R_{tum} = 1.000) at t_{opt} = 114.9 min. This improvement in therapeutic efficacy is attributable to the enhanced MNP diffusion [26,28]. Longer waiting times yield a more uniform MNP volume fraction distribution. The MNP concentrations at the tumor center for the three optimal waiting times are 2.75×10^{-2}, 5.91×10^{-3}, and 2.72×10^{-3}, respectively. The resulting more homogeneous MNP distributions generate progressively more uniform temperature fields, with tumor-center temperatures of 56.6, 48.4, and 46.0°C for three strategies, respectively, while maintaining a constant temperature of 43.0°C at the tumor boundary (see Fig. 5(d)). However, extending the waiting time increases the required MNP dose V_{opt} by 36.9% at t_{opt} = 114.9 min, relative to the baseline one-site strategy.

In practice, increasing the waiting time and MNP dose may introduce operational inefficiencies and elevate the risk of toxicity within the human body [15,16]. Therefore, strategy selection should carefully balance these practical constraints against therapeutic gains. Nonetheless, the substantial improvement in R_{hea} and the significant reduction of the overheated region lead to the strategy with a waiting time of t_{opt} = 114.9 min a promising choice. Thus, this strategy is strongly recommended for magnetic hyperthermia treatment provided that the treatment duration and MNP-related toxicity remain acceptable.

Table 3
Optimal strategies for the eight-site injection case with varying waiting time limits on the spherical tumor model.

Time limit	R_{ium}	R_{hea}	R_{int}	T_{max}, °C	V_{opt}, mm³	t_{opt}, min	d_{opt}, mm
20 min	1.000	1.000	0.800	46.0	1.79	19.3	4.00
30 min	1.000	1.000	0.898	46.0	1.87	29.8	4.02
60 min	1.000	1.000	0.957	46.0	1.97	45.2	3.94

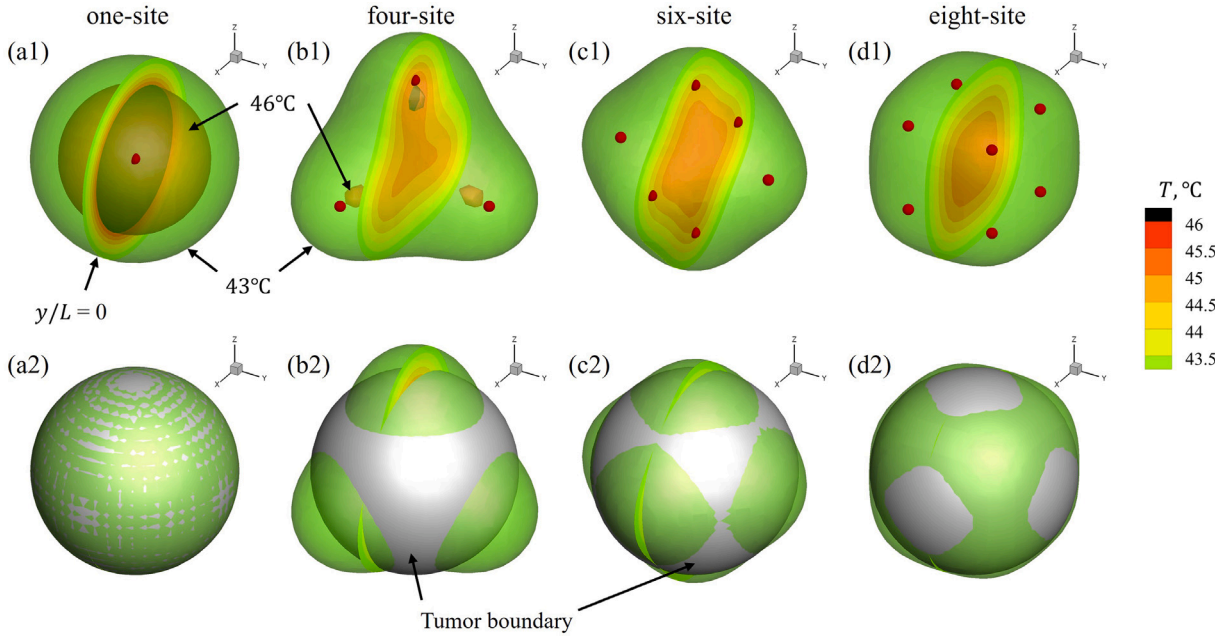

Fig. 4. Optimal spatial temperature distributions for the spherical tumor model with (a) one-site, (b) four-site, (c) six-site, and (d) eight-site injections. The first row shows the temperature field at the mid-plane $y/L = 0$, while the second row compares the 43°C isotherm with the tumor surface (shown in silver). The small red spheres denote the optimal injection sites.

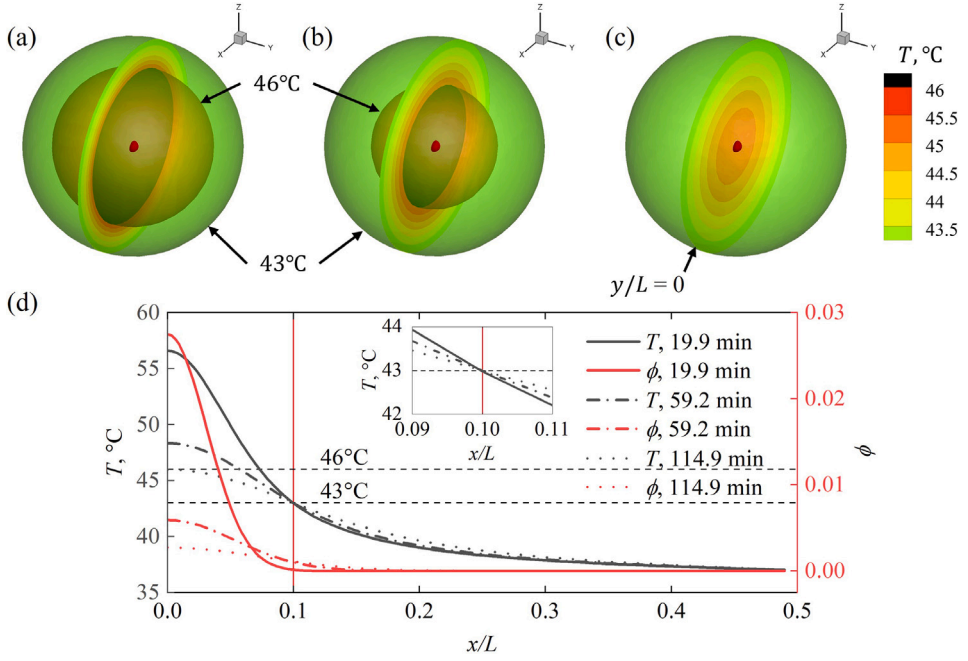

Fig. 5. Optimal spatial temperature distribution for the one-site injection scenarios under three allowed waiting time (20 min, 60 min, and 120 min) for the spherical tumor model, with highlighting on the mid-plane at $y/L = 0$. The optimal waiting times are (a) 19.9 min, (b) 59.2 min, and (c) 114.9 min, respectively, where the small red spheres denote the optimal injection sites. Panel (d) presents the radial temperature and MNP concentration profiles. The red vertical line marks the tumor boundary, and the horizontal black dashed lines denote 43°C and 46°C isotherms.

For the eight-site injection scenario, two extended maximum waiting times (30 and 60 min) are considered in addition to the baseline 20-minute limit. The optimal waiting times t_{opt} are 19.3, 29.8, and 45.2 min, respectively, for the three scenarios. The value t_{opt} = 45.2 min indicates that a 60-minute allowance is non-binding and therefore sufficient for this scenario. As shown in Fig. 6, increasing t_{opt} results in a slight improvement in the temperature field (most notably at the interface), despite substantial variation in the intratumoral MNP distribution (see Figs. 6 (a2) to (c2) and (d)). This adjustment also requires a significant increase in the optimal MNP dose V_{opt}, rising by 10.1% as t_{opt} increases from 19.3 to 45.3 min (see Table 3). Given the increased treatment duration and potential biotoxicity, along with the limited improvement in overall temperature performance, the strategies with t_{opt} = 19.3 and t_{opt} = 45.2 min can be regarded as alternative choices. By comparison, the one-site strategy at t_{opt} = 114.9 min yields a more favorable temperature field, albeit with slightly higher MNP dose than the eight-site strategy at t_{opt} = 45.2 min. The one-site option may also offer greater procedural convenience.

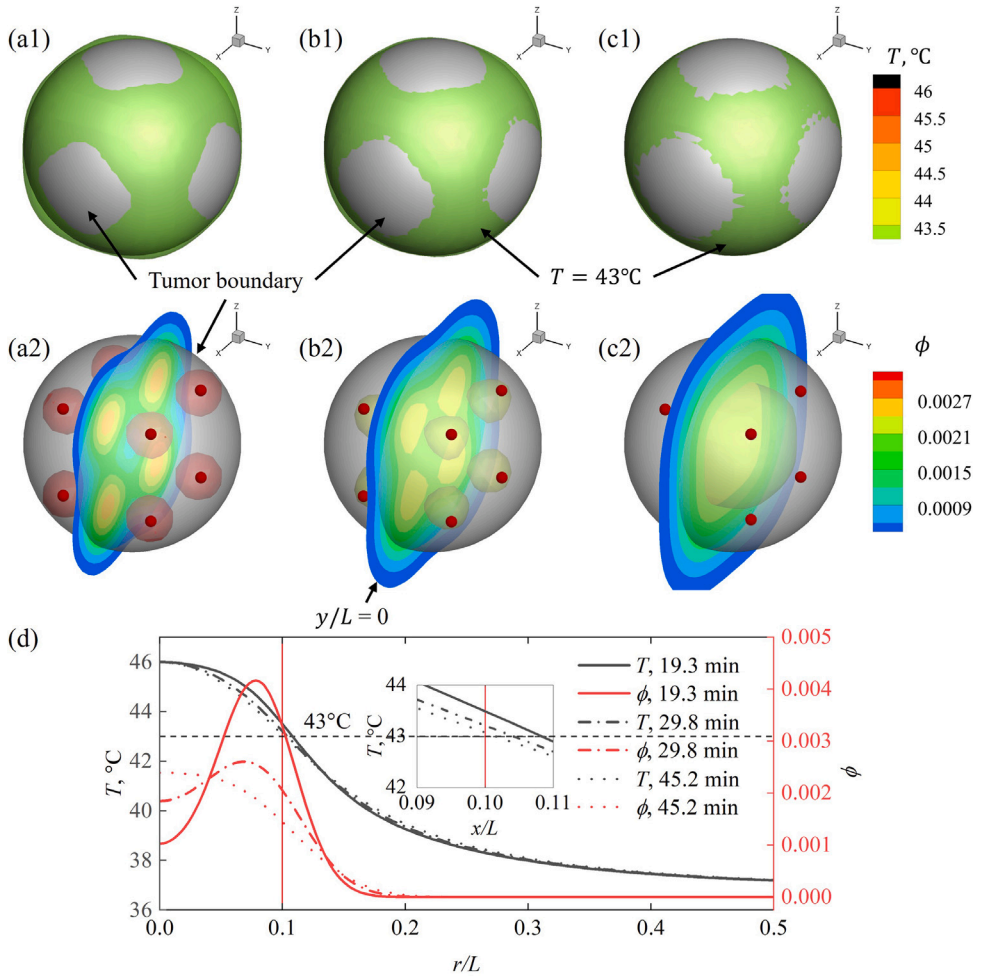

Fig. 6. Optimal spatial temperature and MNP volume fraction distributions for the eight-site injection scenario under three different waiting time limits (20 min, 30 min, and 60 min) for the spherical tumor model. The optimal waiting times are (a) 19.27 min, (b) 29.84 min, and (c) 45.21 min. Panels (a1) ~ (c1) compare the 43°C isotherm with the interface of tumor and healthy tissue. The silver surface representing the tumor boundary. Panels (a2) ~ (c2) depict the MNP volume fraction, highlighting the profile at $y/L = 0$ along with isosurfaces at $\phi = 0.0033$, 0.0024, and 0.0021, respectively, for the three strategies. The small red spheres indicate the injection sites. Panel (d) presents the temperature and MNP concentration profiles along the (1,1,1) direction (the search path of the first injection site) with $r = \sqrt{x^2 + y^2 + z^2}$. The red vertical line marks the tumor boundary, and the black dashed line indicates 43°C.

3.2. Simple irregular tumor

The simple irregular tumor consists of two connected spheres, as presented in Fig. 1. This axisymmetric configuration indicates that the previously assumed centrosymmetric MNP distribution is no longer applicable. To enhance treatment efficacy, injection sites are allowed anywhere within a prescribed cube domain, and the MNP distribution from each injection is independent of the others. Accordingly, each injection is characterized by five independent normalized ratios: $k_{\phi,i}$, $k_{\sigma,i}$, and $(k_{x,i}, k_{y,i}, k_{z,i})$. This section examines one-, two-, and three-site injection scenarios, requiring the determination of five, ten, and fifteen normalized ratios, respectively. A 120-minute waiting-time limit is adopted based on its demonstrated effectiveness for the spherical tumor model (see Section 3.1.2). Consequently, the reference standard derivation is $\sigma_0 = 0.378$, and the reference volume fraction is reduced to $\phi_0 = 0.005$, in accordance with the maximum value indicated in Fig. 5(d). The reference coordinate is set to $(x_0, y_0, z_0) = (4.5, 4.5, 4.5)$ mm, which defines a constrained injection cube that occupies 90% of the side length of the red cube shown in Fig. 1.

Given the rapid convergence observed for the spherical tumor model, the number of generations is reduced to 150 in this section. As the expanded parameter space necessitates a broader exploration, the swarm sizes per generation are set to 20 particles for the one-site injection, 40 for the two-site injection, and 50 for the three-site injection. Fig. 7 presents the searching trajectories for the three scenarios. In general, the completely independent search of normalized ratios produces more possibilities than the symmetric search previously employed for the spherical tumor model. For this simple irregular tumor, the maximum objective values for the two-site and three-site injections are both 0.899, exceeding that of the one-site injection (0.849) by more than 5.9%. The linear-like relationships between the satisfied tumor ratio R_{tum} and the objective function J across all three scenarios are identical to those observed for the spherical tumor model. In both the two-site and three-site injection scenarios, the optimal R_{tum} and R_{hea} effectively meet their targets (1.000 each) with modest MNP doses (2.40 and 2.46 mm^3, respectively).

As shown in Fig. 8, all three scenarios exhibit quick convergence despite the large number of independent optimization parameters, each attaining its optimum within 75 generations, thereby confirming the suitability of the PSO settings. Notably, several parameters converge to similar values between Figs. 8(b) and (c), while others approach 0, which together indicate substantial similarity between the two strategies. This resemblance is further illustrated in the optimal spatial temperature fields plotted in Fig. 9. For the one-site strategy, the 43°C isotherm is nearly spherical and deviates markedly from the tumor boundary, resulting in an unsatisfactory intratumoral temperature distribution. Adding injections significantly improves temperature

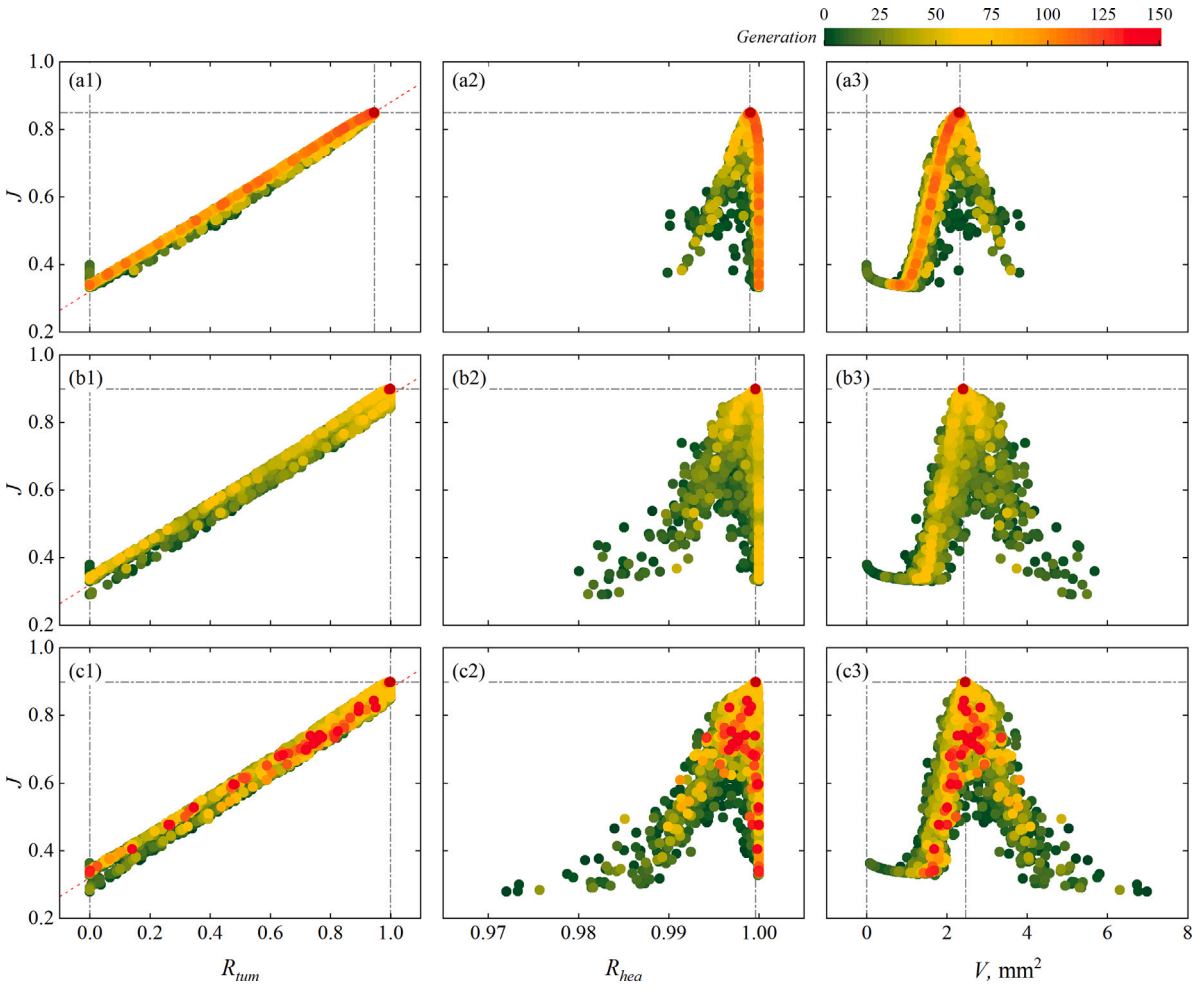

Fig. 7. Optimization trajectory for the simple irregular tumor model, including the satisfied tumor ratio R_{tum}, the satisfied healthy tissue ratio R_{hea}, and the required volume of MNP V, for the scenarios:(a1)~(a3) one-site injection, (b1)~(b3) two-site injection, and (c1)~(c3) three-site injection, respectively. The dark red point indicates the optimal choice.

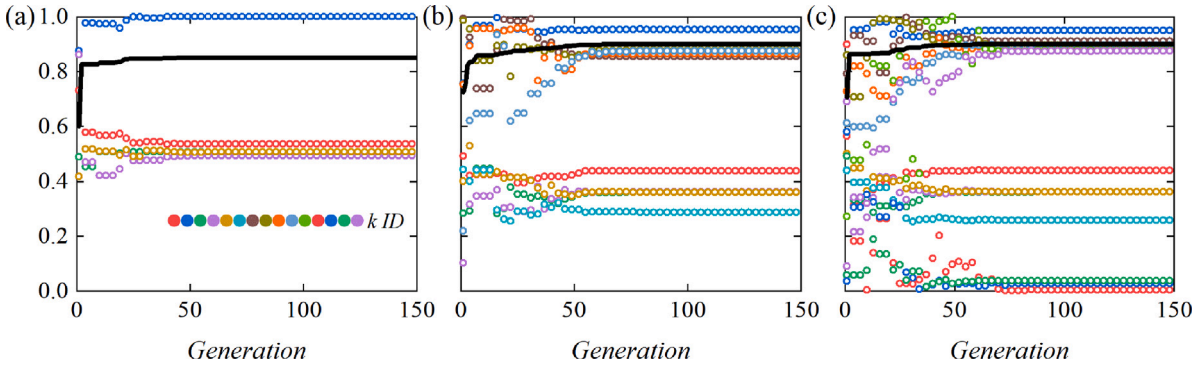

Fig. 8. PSO convergence process for the simple irregular tumor model with (a) one-site injection, (b) two-site injection, (c) three-site injection. Symbols denote the evolution of optimal normalized ratios $k_{\phi,i}$, $k_{\sigma,i}$ and $(k_{x,i}, k_{y,i}, k_{z,i})$, where i represents the ith injection. Each scenario involves a total of $5n$ parameters.

performance in both the two-site and three-site strategies. The similarity between these two strategies is evidenced by the shape of the 43°C isotherm, the temperature distribution on the mid-plane $y/L = 0$, and the locations of the two intratumoral injection sites.

Table 4 summarizes the three optimal strategies for the different injection numbers. Compared to the one-site strategy, the gains achieved by the two- and three-site strategies primarily arise from substantial increases in R_{tum} and R_{int}. The close similarity between these two strategies is also evident in their scores across the four performance indicators and further extends to the optimal physical variables, namely, maximum temperature T_{max}, optimal waiting times $t_{opt,i}$ (i = 1, 2), MNP doses $V_{opt,i}$, and the coordinates (x_i, y_i, z_i) of the first two injection sites. Although the three-site strategy formally includes a third injection, its contribution to the total MNP dose is negligible (7.60×10^{-5}%), so that the three-site strategy effectively reduces to a practical two-site strategy, mirroring the optimal injection number reported by Salloum

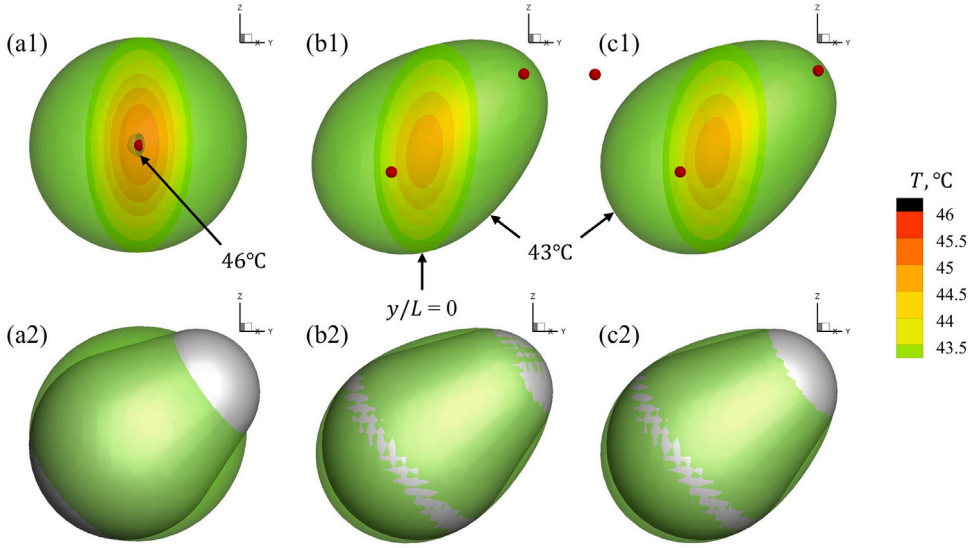

Fig. 9. Optimal spatial temperature distributions for the simple irregular tumor model with (a) one-site, (b) two-site, and (c) three-site injections. The first row shows the temperature field at the mid-plane $y/L = 0$, while the second row compares the 43°C isotherm with the tumor surface (shown in silver). The small red spheres indicate the optimal injection sites.

Table 4
Optimal strategies for the one-site, two-site, three-site injection scenarios applied to the simple irregular tumor model.

Injection strategy	one-site	two-site		three-site		
J	0.849	0.899		0.899		
R_{tum}	0.947	0.999		1.000		
R_{hea}	0.999	1.000		1.000		
R_{int}	0.620	0.856		0.862		
R_{dose}	0.144	0.135		0.131		
T_{max}, °C	46.1	45.4		45.4		
$t_{opt,i}$, min	119.92	109.2	87.8	108.2	99.5	1.6×10^{-2}
$V_{opt,i}$, mm^3	2.31	1.63	0.77	1.62	0.84	1.87×10^{-7}
V_{opt}, mm^3	2.31	2.40		2.46		
(x_1, y_1, z_1), mm	(0.07, −0.07, 0.07)	(−1.26, −1.24, −1.25)		(−1.25, −1.24, −1.24)		
(x_2, y_2, z_2), mm	–	(3.41, 3.28, 3.38)		(3.55, 3.52, 3.55)		
(x_3, y_3, z_3), mm	–	–		(−4.25, −4.16, 3.37)		

et al. [32] and consistent with the axisymmetric geometry of the tumor shape and the resulting two-site MNP distribution.

3.3. Complex irregular tumor

The complex irregular tumor consists of three connected spheres, producing an asymmetric shape and representing a more general scenario. Optimization settings are maintained as in the simple irregular tumor model, and three injection scenarios are evaluated: one-site, two-site, and three-site injections.

Fig. 10 shows the evolution of the normalized ratios $k_{\phi,i}$, $k_{\sigma,i}$ and $(k_{x,i}, k_{y,i}, k_{z,i})$, and the objective function J for the three injection scenarios. As for the simple irregular tumor model, the optimization employs 150 generations, with swarm sizes of 20, 40, and 50 particles for the one-, two-, and three-site cases, respectively. Although the increased parameter space requires more generations for convergence, all three scenarios reach their optima within 100 generations.

The optimal temperature distributions for the three scenarios are shown in Fig. 11. Evidently, temperature performance improves with increasing injection number, with the three-site strategy achieving the best outcome. In this complex, asymmetric tumor geometry, the centrosymmetric and axisymmetric temperature fields produced by the one-site and two-site injection strategies, respectively, are inherently less effective. Accordingly, the objective function J increases substantially for the three-site strategy, from 0.850 (one-site) and 0.857 (two-site) to 0.891 (three-site). This improvement is driven principally by marked increases in R_{tum} and R_{int} (see Table 5). Table 5 also lists the optimal physical variables for the three-site strategy, including a maximum temperature $T_{max} = 45.4$°C (within a clinically acceptable range), an optimal total MNP dose $V_{opt} = 2.19$ mm^3 (the lowest among the three strategies), and the optimal injection sites.

3.4. Geometry-dependent injection strategy

Across the three investigated tumor models, the optimal injection number depends on tumor geometry and can be inferred from the number of connected spheres. In practice, geometric decomposition of tumor morphology using Computerized Tomography (CT) can determine the number and sizes of connected spheres that best approximate the actual tumor shape. Incorporating this decomposition into the optimization workflow can substantially improve the efficiency of the optimization search.

The results in Table 6 indicate that the optimal injection sites S_i are closely related to the sphere centers O_i and their radii R_i. Here, $\overrightarrow{OO_i}$ denotes the vector from the tumor center (O, the coordinate origin) to the ith sphere center (O_i), and $\overrightarrow{OS_i}$ represents the vector from O to the ith optimal injection site (S_i). Consequently, the ratios $\overrightarrow{OS_i} \cdot \overrightarrow{OO_i}/(|\overrightarrow{OS_i}\| \overrightarrow{OO_i}|)$ and $\overrightarrow{OS_i} \cdot \overrightarrow{OO_i}/|\overrightarrow{OO_i}|^2$ measures the relative direction (1 and −1 correspond to identical and opposite direction, respectively) and normalized projection length (1 indicates equal lengths) of $\overrightarrow{OS_i}$ compared to $\overrightarrow{OO_i}$, respectively. The spherical tumor model is excluded

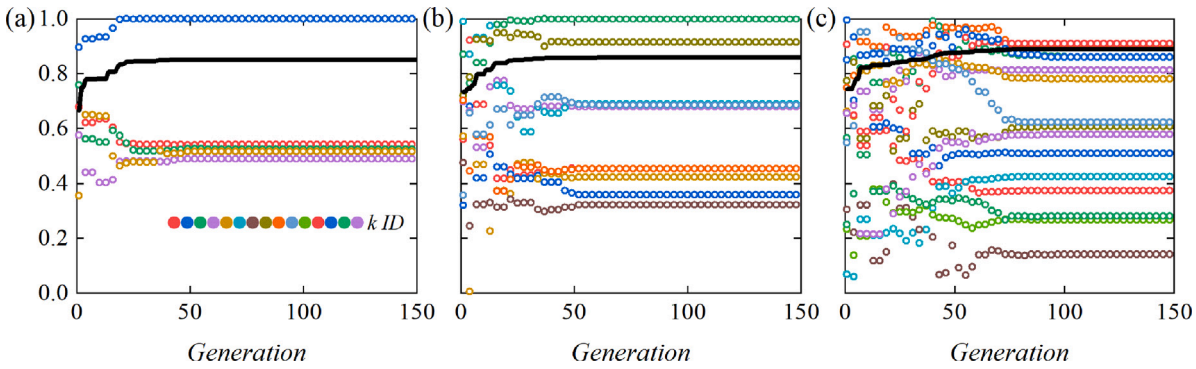

Fig. 10. PSO searching process for the complex irregular tumor model with (a) one-site injection, (b) two-site injection, and (c) three-site injection. Symbols denote the evolution of optimal normalized ratios $k_{\phi,i}$, $k_{\sigma,i}$ and $(k_{x,i}, k_{y,i}, k_{z,i})$, where i denotes the ith injection. Each scenario involves a total of $5n$ parameters.

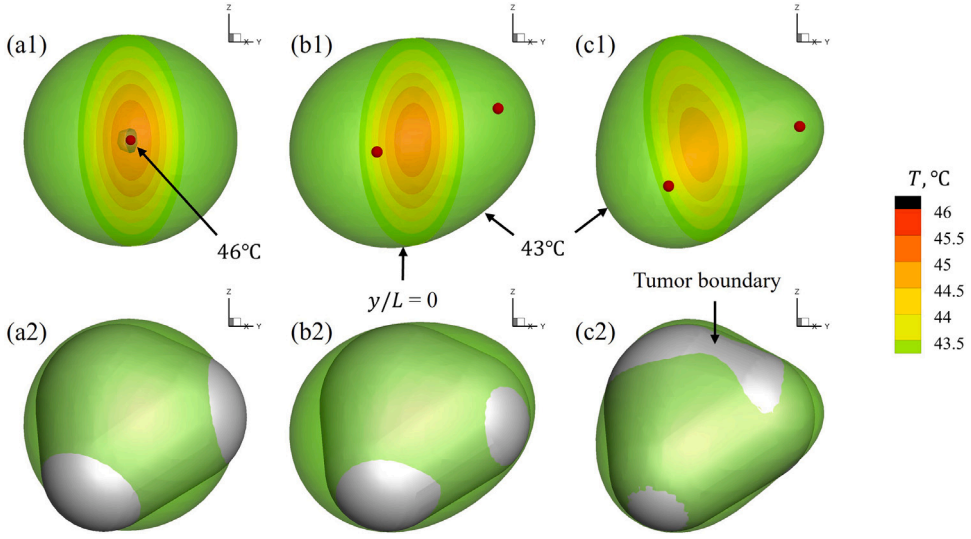

Fig. 11. Optimal spatial temperature distribution for the complex irregular tumor model with (a) one-site, (b) two-site, and (c) three-site injections. The first row shows the temperature field at the mid-plane $y/L = 0$, while the second row compares the 43°C isotherm with the tumor surface, which is depicted in silver. The little red spheres indicate the optimal injection sites.

Table 5
Optimal strategies for the one-site, two-site, and three-site injection scenarios applied to the complex irregular tumor model.

Injection strategy	one-site	two-site		three-site		
J	0.850	0.857		0.891		
R_{ium}	0.956	0.978		0.994		
R_{hea}	0.999	0.999		0.999		
R_{int}	0.586	0.557		0.779		
R_{dose}	0.143	0.134		0.156		
T_{max}, °C	46.1	46.0		45.4		
$t_{opt,i}$, min	119.8	119.6	55.4	79.1	73.2	21.6
$V_{opt,i}$, mm^3	2.32	1.94	0.18	0.86	1.04	0.28
V_{opt}, mm^3	2.32	2.42		2.19		
(x_1, y_1, z_1), mm	(0.22, −0.11, 0.14)	(−0.69, −1.60, −0.40)		(−3.16, 1.08, 3.20)		
(x_2, y_2, z_2), mm	–	(1.70, −3.72, 1.67)		(1.00, −2.19, −2.05)		
(x_3, y_3, z_3), mm	–	-		(3.51, 3.63, 0.83)		

from this comparison because, in that case, the sphere center and the optimal injection site coincide.

As shown in Table 6, the direction ratio $\overrightarrow{OS_i} \cdot \overrightarrow{OO_i}/(|\overrightarrow{OS_i}\| \overrightarrow{OO_i}|)$ is very close to 1 for each injection, indicating a strong alignment between the directions of the optimal injection sites and the corresponding sphere centers. The perfect (100%) correlation observed for the simple irregular tumor model is primarily attributed to the axisymmetry of both the tumor shape and the coaxial MNP distribution. In the complex tumor model, each injection site achieves a direction ratio above 0.97, demonstrating that pronounced directional alignment persists even in more general, non-symmetric geometries. Fig. 12 further illustrates this alignment. The length ratio $\overrightarrow{OS_i} \cdot \overrightarrow{OO_i}/|\overrightarrow{OO_i}|^2$ exceeds 1 in all cases, indicating that $\overrightarrow{OS_i} > \overrightarrow{OO_i}$. In other words, optimal injection sites are displaced radially outward relative to the sphere centers, which likely serves to mitigate intratumoral overheating, consistent with previous findings [24,54]. Furthermore, the length ratio generally increases with sphere radius, suggesting that injections are placed progressively farther from the tumor center as sphere size grows.

Table 6
Comparison of the vectors to the sphere centers $\overrightarrow{OO_i}$ and the injection sites $\overrightarrow{OS_i}$, where i denotes the injection index. The ratios $\overrightarrow{OS_i} \cdot \overrightarrow{OO_i}/(|\overrightarrow{OS_i}||\overrightarrow{OO_i}|)$ and $\overrightarrow{OS_i} \cdot \overrightarrow{OO_i}/|\overrightarrow{OO_i}|^2$ illustrate the relative direction and length, respectively.

Model & Strategy	R_i, mm	$\overrightarrow{OS_i} \cdot \overrightarrow{OO_i}/(\|\overrightarrow{OS_i}\|\|\overrightarrow{OO_i}\|)$	$\overrightarrow{OS_i} \cdot \overrightarrow{OO_i}/\|\overrightarrow{OO_i}\|^2$
Simple irregular two-site	4.5	1.00	2.50
	3	1.00	1.68
Complex irregular three-site	4.5	0.97	3.18
	3	1.00	1.05
	3.25	1.00	2.02

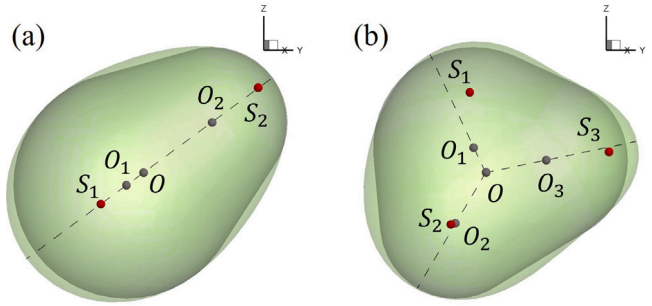

Fig. 12. Comparison of the optimal injection sites and the spherical centers for both simple and complex irregular tumor shapes. The small black dots denote the tumor center (O, coordinate origin) and sphere centers (O_i, $i = 1, 2$ for simple irregular tumor and $i = 1, 2, 3$ for complex irregular tumor). The small red spheres denote injection sites (S_i). The dashed lines connect the tumor center and sphere centers.

Overall, the observed alignment in both direction and length provides a useful guideline for selecting and evaluating candidate injection sites in practical implementations.

4. Conclusions

This study investigates optimal MNP injection strategies in 3D configurations to better approximate clinical conditions and thereby maximize the efficacy of magnetic hyperthermia. The 3D PBHTE is used for bio-heat simulations, and PSO is employed to identify optimal MNP distributions. Optimization outcomes are evaluated primarily by thermal performance while simultaneously accounting for total MNP dose. Three tumor geometries are considered: spherical, simple irregular, and complex irregular, spanning a range from complete symmetry to progressively increasingly generalized, non-symmetric shapes. Each scenario converges rapidly and yields reasonably satisfactory results, demonstrating the efficiency and effectiveness of this framework for optimizing treatment efficacy.

For the spherical tumor model, waiting time significantly influences the optimization outcomes. Although the one-site MNP distribution is consistent with tumor symmetry, its short optimal time ($t_{opt} = 19.9$ min) limits MNP diffusion and results in a large overheated intratumoral volume (39.8%). Multi-site strategies improve temperature control, with the eight-site strategy achieving the best performance under short waiting times. However, when the optimal waiting time is extended to $t_{opt} = 114.9$ min, sufficient MNP diffusion prevents overheating and highlights the benefits of the centrosymmetric configuration, making the one-site strategy highly recommended, provided the prolonged duration and MNP dose are acceptable. By contrast, extending the waiting time for the eight-site strategy yields only marginal temperature improvements while substantially increasing treatment duration and risk of MNP-related toxicity.

Motivated by the improved performance associated with prolonged waiting times and by the increased geometric complexity, the irregular tumor scenarios adopt an extended waiting time limit (120 min) and optimize each MNP injection independently to enhance thermal control. The rapid convergence observed confirms the capability and suitability of the framework in managing the enlarged parameter space. For the simple irregular tumor, the two-site and three-site scenarios produce nearly identical optimal outcomes, both in objective indicators and in the optimal physical variable, owing to the degradation of the third injection in the three-site strategy. These results indicate that the two-site strategy is optimal for the simple irregular tumor. Similarly, the three-site strategy is most suitable for the complex irregular tumor.

Therefore, the optimal number of injections correlates with the number of connected spheres, a relationship driven primarily by tumor geometry and the corresponding optimal MNP-induced temperature distribution. This observation provides a practical guideline for selecting the injection number once the connected sphere decomposition has been obtained from CT imaging. Moreover, the vectors from the tumor center to the optimal injection sites closely align with those to the centers of the connected spheres, and their length generally increases with sphere radius. Hence, the center-to-site vectors provide an effective reference for evaluating or predicting the optimal strategy, especially when a full optimization routine is not available.

This work is valuable for optimizing treatment efficacy across a range of tumor geometries. The observed trends and findings provide deeper insights into the optimization presets and strategy evaluation, thereby contributing to improved planning of magnetic hyperthermia treatments. However, while the three tumor models serve as representative examples of the majority of tumors encountered, they cannot fully replicate each real tumor due to its unique characteristics. In future work, topology analysis could be integrated into the efficient and effective determination of the most representative computational model. Furthermore, although the treatment almost achieves the desired efficacy, 0.4% of tumor cells remain undestroyed, and 0.1% of healthy tissue is affected in the scenario with the complex irregular tumor model. Therefore, allowing dynamic adjustment of the injection number during the optimization process, such as increasing injections in the unablated tumor regions and reducing injections in areas where healthy tissue is impacted, could enhance the flexibility of the optimization search and potentially improve treatment efficacy, especially for complex clinical scenarios, such as tumors adjacent to blood vessels, bone, or the skin surface. Additionally, the use of simplified tumor geometries, constant thermal properties for tumor and healthy tissues, and an empirical model for perfusing blood may limit the fidelity of our approximation to clinical conditions. Refining these aspects represents other directions for our future research.

CRediT authorship contribution statement

Qian Jiang: Writing – review & editing, Writing – original draft, Visualization, Validation, Software, Methodology, Investigation, Formal analysis, Conceptualization. **Zhaokun Wang:** Writing – review & editing, Methodology. **Feng Ren:** Writing – review & editing, Methodology. **Chenglei Wang:** Writing – review & editing, Methodology. **Gholamreza Kefayati:** Writing – review & editing, Methodology. **Sasa Kenjeres:** Writing – review & editing. **Kambiz Vafai:** Writing – review & editing. **Xinguang Cui:** Writing – review & editing. **Yang Liu:** Writing – review & editing, Supervision. **Hui Tang:** Writing – review & editing, Visualization, Supervision, Methodology, Investigation, Funding acquisition, Conceptualization.

Declaration of competing interest

The authors declare that they have no known competing financial interests or personal relationships that could have appeared to influence the work reported in this paper.

Acknowledgment

This study was financially supported by the Research Grants Council of Hong Kong under General Research Fund (Project No. 15214418).

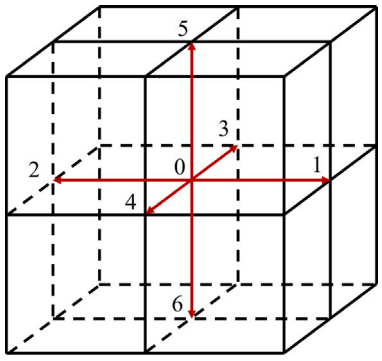

Fig. A.1. Lattice arrangement for D3Q7.

Appendix A. Solving PBHTE using LBM

The lattice Boltzmann method (LBM) is a mesoscopic computational fluid dynamics (CFD) approach, deriving from lattice gas automata (LGA). LBM has been effectively utilized in modeling fluid flow and heat/mass transfer simulations [55–57]. Initially applied to magnetic hyperthermia by Zhang [58], LBM has demonstrated significant capability in addressing bioheat transfer issues, thereby promoting its broader adoption in this field [28,59,60]. In this work, the multiple-relaxation-time lattice Boltzmann method (MRT-LBM) is employed owing to its established numerical stability at low viscosity [61,62].

The D3Q7 scheme is recommended for solving the 3D energy equation and other scalar equations [63]. In this scheme, there are seven velocity vectors in the lattice, as shown in Fig. A.1. The discrete D3Q7 MRT-LBM equation for temperature field is given by [64–66]

$$\mathbf{g}(x_k+\mathbf{e}\delta_t, t_n+\delta_t)-\mathbf{g}(x_k,t_n) = -\mathbf{N}^{-1}\boldsymbol{\Theta}[\mathbf{n}-\mathbf{n}^{(eq)}]|_{(x_k,t_n)}+\mathbf{N}^{-1}\delta_t(\mathbf{I}-\frac{\boldsymbol{\Theta}}{2})\boldsymbol{\Psi}, \quad \text{(A.1)}$$

where $\mathbf{g}(x_k,t_n)=(g_0(x_k,t_n), g_1(x_k,t_n),\dots,g_6(x_k,t_n))^T$ is distribution function vectors at time t_n and node x_k. $\mathbf{n}$ and $\mathbf{n}^{(eq)}$ represent the moment vectors and their corresponding equilibrium moment vectors, respectively. $\mathbf{e}$ denotes unit velocities along seven discrete directions.

$$e_i = \begin{cases} (0,0,0), & i=0 \\ (\pm1,0,0),(0,\pm1,0),(0,0,\pm1), & i=1\sim 6. \end{cases} \quad \text{(A.2)}$$

$\mathbf{N}$ is a 7×7 orthogonal transformation matrix

$$\mathbf{N} = \begin{pmatrix} 1 & 1 & 1 & 1 & 1 & 1 & 1 \\ 0 & 1 & -1 & 0 & 0 & 0 & 0 \\ 0 & 0 & 0 & 1 & -1 & 0 & 0 \\ 0 & 0 & 0 & 0 & 0 & 1 & -1 \\ 6 & -1 & -1 & -1 & -1 & -1 & -1 \\ 0 & 2 & 2 & -1 & -1 & -1 & -1 \\ 0 & 0 & 0 & 1 & 1 & -1 & -1 \end{pmatrix}, \quad \text{(A.3)}$$

and

$$\mathbf{n}=\mathbf{N}\mathbf{g},\ \mathbf{g}=\mathbf{N}^{-1}\mathbf{n}. \quad \text{(A.4)}$$

The equilibrium distribution function $g_i^{(eq)}$ $(i=0,1,\dots,6)$ is defined as [64,65]

$$g_i^{(eq)} = \bar{\omega}_i T(1+\frac{\mathbf{e_i}\cdot\mathbf{u}}{c_{sT}^2}), \quad \text{(A.5)}$$

where $c_{sT}^2=c^2/4$ is the sound speed. $\bar{\omega}_i$ is the weight coefficient, which is given by

$$\bar{\omega}_i = \begin{cases} 1/4, & i=0 \\ 1/8, & i=1\sim 6. \end{cases} \quad \text{(A.6)}$$

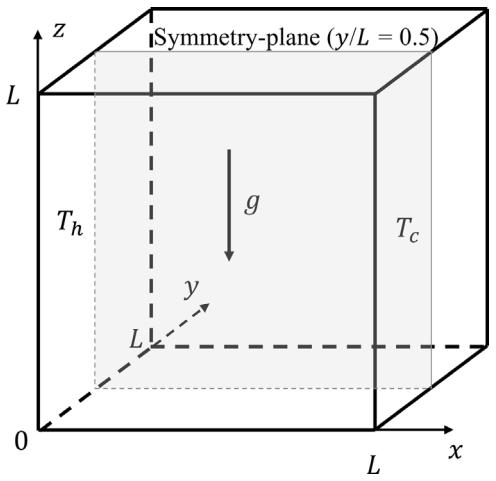

Fig. A.2. Schematic of natural convection in Liu et al. [64].

Table A.1
Sensitivity studies on the grid number and computational domain size in 3D configuration.

Grid number	$N_x\times N_y$	T_c,°C	T_r,°C	Err_c,%	Err_r,%
	$50\times50\times50$	45.82	42.55	0.33	0.26
	$100\times100\times100$	45.97	42.66	0.06	0.06
	$200\times200\times200$	45.99	42.69	–	–
Domain size	L/l	T_c,°C	T_r,°C	Err_c,%	Err_r,%
	5	45.97	42.66	0.22	0.24
	10	46.07	42.77	–	–

$\boldsymbol{\Theta}$ is a diagonal relaxation matrix, as

$$\boldsymbol{\Theta} = \mathrm{diag}(1, 1/\tau_T, 1/\tau_T, 1/\tau_T, 1.2, 1, 1), \quad \text{(A.7)}$$

where τ_T is linked to the effective thermal diffusivity in Chapman–Enskog analysis, as

$$\alpha_e = c_{sT}^2(\tau_T-0.5)\delta_t. \quad \text{(A.8)}$$

The macroscopic is obtained by

$$T=\sum_{i=0}^{6} g_i + \frac{1}{2}\delta_t Q \quad \text{(A.9)}$$

An investigation of natural convection in a cubic cavity is conducted to validate the D3Q7 MRT-LBM framework for solving the temperature field. Fig. A.2 presents the schematic, where all boundaries are fixed. The left and right vertical walls are maintained at constant temperatures of T_h and T_c, respectively, while the remaining walls are adiabatic. The flow within the cavity is incompressible and driven by buoyancy forces, and it is solved using the D3Q19 scheme. The temperature profile on the mid-plane ($y/L=0$), shown in Fig. A.3, demonstrates good agreement with previously reported data [64]. A comparison with the experiment reported by Moroz et al. [67] is presented in Fig. A.4. This study implemented magnetic hyperthermia in rabbit liver: each rabbit received a 1 mm tumor implant, and four MNP dose groups (25, 50, 75, and 100 mg) were evaluated. A total of 20 rabbits were used, equally distributed among the four groups. Fig. A.4(a) compares the mean temporal temperature evolution at the tumor core. The numerical results agree well with the experimental mean values, and the small deviations observed are likely attributable to uncontrollable experimental uncertainties and operational errors in such small-scale measurements. As illustrated in Fig. A.4(b), the numerical temperature increases at $t=5$ min lie within the experimental error range and are close to the measured mean values, thereby demonstrating the reliability and accuracy of the present framework.

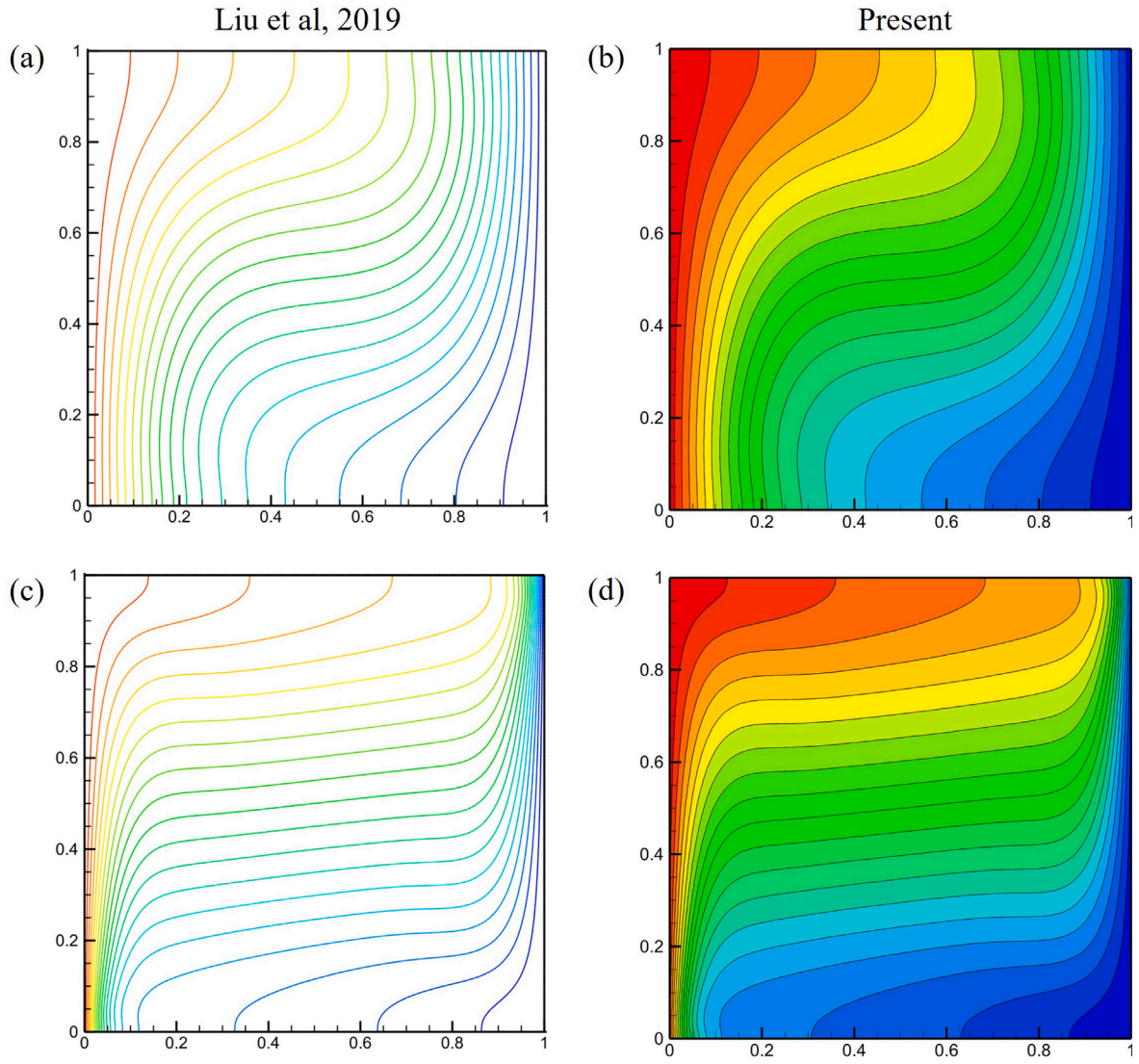

Fig. A.3. Comparison of temperature distributions at $Ra \cdot Da = 10^3$ and $\varphi = 0.8$: (a) - (b) $Ra = 10^4$, $Da = 10^{-1}$; (c) - (d) $Ra = 10^6$, $Da = 10^{-3}$ [64].

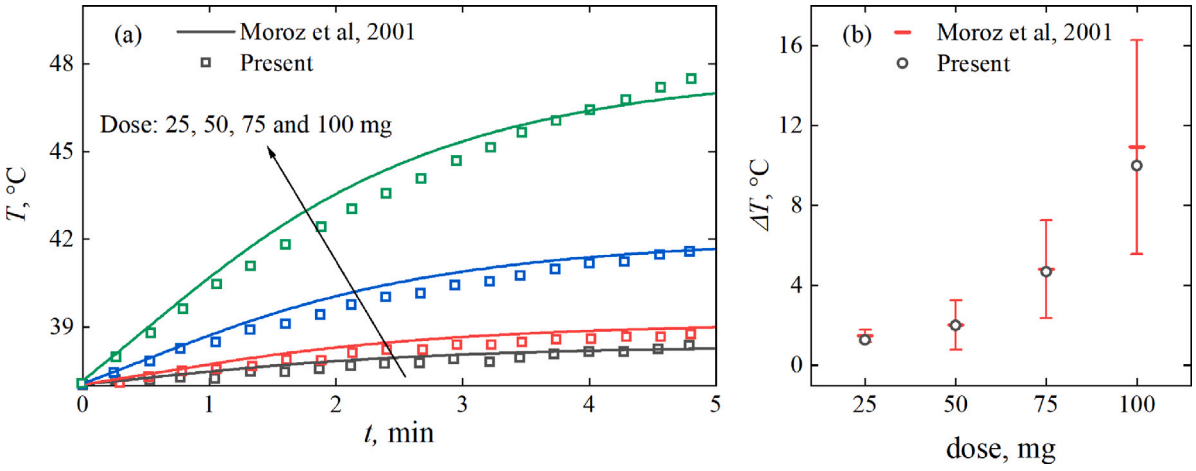

Fig. A.4. Validation against a magnetic hyperthermia experiment in rabbit liver [67].

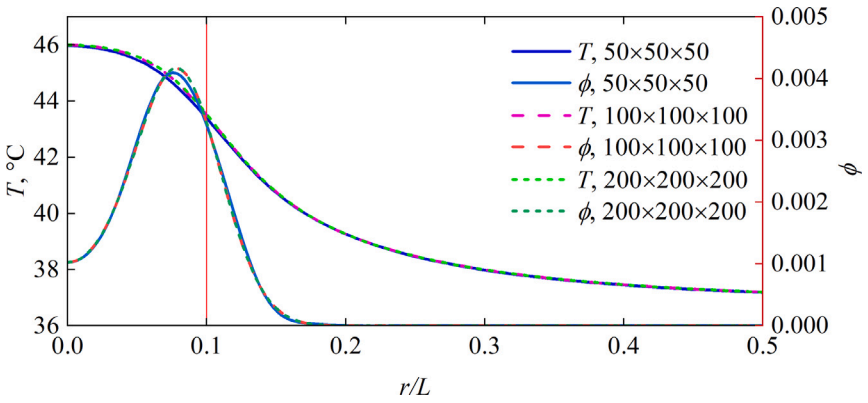

Fig. A.5. Temperature and MNP concentration profiles along the direction of the vector (1,1,1) for the various mesh resolutions, where $r = \sqrt{x^2 + y^2 + z^2}$. The red vertical line marks the tumor boundary.

To evaluate the spatial resolution, the optimal eight-site strategy for the spherical tumor model is employed as an example with three sets of meshes: 50 × 50 × 50, 100 × 100 × 100, and 200 × 200 × 200. Fig. A.5 presents a comparison of the three mesh resolutions along the direction (1,1,1), where the most spatial variation in MNP distribution is observed, as indicated in Fig. 6 (a2)~(c2). It is evident from Fig. A.5 that both temperature and MNP concentration exhibit only marginal differences among the three mesh resolutions, particularly between the 100 × 100 × 100 mesh and 200 × 200 × 200 mesh. To quantify these differences, the temperatures at two monitored points, including the tumor center (T_c) and the rightmost point of the tumor boundary (T_r), together with the corresponding errors (Err_c and Err_r), are detailed in Table A.1. The comparison indicates that the 50 × 50 × 50 mesh is adequate for capturing the temperature field; however, to achieve better resolution, the 100 × 100 × 100 mesh is selected for this work. In addition, we assess whether the tissue block is sufficiently large to neglect the influence of boundary conditions by doubling its length. As shown in Table A.1, the results for the original domain size ($L/l = 5$) exhibit almost no difference in temperature at monitored points (below 0.3%) compared to those for the doubled size ($L/l = 10$), indicating that the domain size used in this work is adequate.

Appendix B. Particle swarm optimization

Particle swarm optimization (PSO) is a stochastic, population-based heuristic optimization algorithm that makes few assumptions and can efficiently handle multimodal problem together with the large search spaces [53,68]. PSO is inspired by collective swarm behaviors, such as insect colonies, bird flocking, fish schooling, and animal herding, in which individuals search collaboratively by using both their own experience and information shared by others [69]. The update of each particle at a given iteration is governed by its accumulated knowledge, social communication with other particles, and the inertia, which together drive the swarm toward the optimization objective [70]. Over the years PSO has been extended into multiple variants and has been successfully applied to a wide range of problems [68,71–76]

This work employs a scheme with a linearly decreasing inertia weight [75], which promotes global search during the initial iterations and gradually shifts toward local exploitation, thereby ensuring both global optimality and rapid convergence. The position x of the ith particle in parameter space at time $t + 1$, and its corresponding value change (velocity) v, can be expressed as

$$x^{t+1} = v^t + x^t \tag{B.1a}$$

$$v^{t+1} = wv^t + c_1 r_1 (p^t - x^t) + c_2 r_2 (g^t - x^t) \tag{B.1b}$$

where w denotes the inertia weight. c_1 and c_2 are acceleration constants that scale the stochastic cognitive and social components, which pull each particle toward its personal best and the global best positions, respectively. In this work, w decreases linearly from 0.8 to 0, while c_1 and c_2 are fixed at 1.5. r_1 and r_2 are independent random variables in $[0, 1]$. p and g denote the personal best position of the present particle and the global best position of the swarm, respectively. The algorithm has been validated on multimodal benchmark functions, and its efficiency and capability for optimizing MNP distributions to maximize magnetic hyperthermia efficacy have been demonstrated (see our previous work [38] for details).

Data availability

Data will be made available on request.

References

[1] S. Sharma, N. Shrivastava, F. Rossi, N.T.K. Thanh, et al., Nanoparticles-based magnetic and photo induced hyperthermia for cancer treatment, Nano Today 29 (2019) 100795.
[2] V. Vilas-Boas, F. Carvalho, B. Espiña, Magnetic hyperthermia for cancer treatment: main parameters affecting the outcome of in vitro and in vivo studies, Molecules 25 (12) (2020) 2874.
[3] J. Jose, R. Kumar, S. Harilal, G.E. Mathew, D.G.T. Parambi, A. Prabhu, M. Uddin, L. Aleya, H. Kim, B. Mathew, et al., Magnetic nanoparticles for hyperthermia in cancer treatment: an emerging tool, Environ. Sci. Pollut. Res. 27 (16) (2020) 19214–19225.
[4] M. Liangruksa, R. Ganguly, I.K. Puri, Parametric investigation of heating due to magnetic fluid hyperthermia in a tumor with blood perfusion, J. Magn. Magn. Mater. 323 (6) (2011) 708–716.
[5] P. Das, M. Colombo, D. Prosperi, Recent advances in magnetic fluid hyperthermia for cancer therapy, Colloids Surf. B 174 (2019) 42–55.
[6] C.S. Kumar, F. Mohammad, Magnetic nanomaterials for hyperthermia-based therapy and controlled drug delivery, Adv. Drug Deliv. Rev. 63 (9) (2011) 789–808.
[7] M. Johannsen, U. Gneveckow, K. Taymoorian, B. Thiesen, N. Waldöfner, R. Scholz, K. Jung, A. Jordan, P. Wust, S. Loening, Morbidity and quality of life during thermotherapy using magnetic nanoparticles in locally recurrent prostate cancer: results of a prospective phase I trial, Int. J. Hyperth. 23 (3) (2007) 315–323.
[8] C.-T. Lin, K.-C. Liu, Estimation for the heating effect of magnetic nanoparticles in perfused tissues, Int. Commun. Heat Mass Transfer 36 (3) (2009) 241–244.
[9] M.A. Giordano, G. Gutierrez, C. Rinaldi, Fundamental solutions to the bioheat equation and their application to magnetic fluid hyperthermia, Int. J. Hyperth. 26 (5) (2010) 475–484.
[10] C.-y. Yang, Determining the heat strength required in hyperthermia treatments, Int. Commun. Heat Mass Transfer 57 (2014) 282–285.
[11] J. Ma, X. Yang, Y. Sun, J. Yang, Theoretical investigation on the thermo-mechanical responses of the human skin during thermal therapy, Int. J. Mech. Sci. 161 (2019) 105041.
[12] S. Laurent, D. Forge, M. Port, A. Roch, C. Robic, L. Vander Elst, R.N. Muller, Magnetic iron oxide nanoparticles: synthesis, stabilization, vectorization, physicochemical characterizations, and biological applications, Chem. Rev. 108 (6) (2008) 2064–2110.

[13] I. Hilger, W.A. Kaiser, Iron oxide-based nanostructures for MRI and magnetic hyperthermia, Nanomedicine 7 (9) (2012) 1443–1459.
[14] H. Liu, J. Zhang, X. Chen, X.-S. Du, J.-L. Zhang, G. Liu, W.-G. Zhang, Application of iron oxide nanoparticles in glioma imaging and therapy: from bench to bedside, Nanoscale 8 (15) (2016) 7808–7826.
[15] M. Ahamed, H. A. Alhadlaq, J. Alam, M. Khan, D. Ali, S. Alarafi, Iron oxide nanoparticle-induced oxidative stress and genotoxicity in human skin epithelial and lung epithelial cell lines, Curr. Pharm. Des. 19 (37) (2013) 6681–6690.
[16] D. Karponis, M. Azzawi, A. Seifalian, An arsenal of magnetic nanoparticles; perspectives in the treatment of cancer, Nanomedicine 11 (16) (2016) 2215–2232.
[17] D. Chang, M. Lim, J.A. Goos, R. Qiao, Y.Y. Ng, F.M. Mansfeld, M. Jackson, T.P. Davis, M. Kavallaris, Biologically targeted magnetic hyperthermia: potential and limitations, Front. Pharmacol. 9 (2018) 831.
[18] T.K. Houlding, E.V. Rebrov, Application of alternative energy forms in catalytic reactor engineering, Green Process. Synth. 1 (2012) 19–31.
[19] C. Sun, J.S. Lee, M. Zhang, Magnetic nanoparticles in MR imaging and drug delivery, Adv. Drug Deliv. Rev. 60 (11) (2008) 1252–1265.
[20] I. Astefanoaei, A. Stancu, Thermo-fluid porosity-related effects in the magnetic hyperthermia, Eur. Phys. J. Plus 136 (12) (2021) 1216.
[21] I. Astefanoaei, A. Stancu, H. Chiriac, Numerical simulation of the temperature field in magnetic hyperthermia with Fe-Cr-Nb-B magnetic particles, Eur. Phys. J. Plus 132 (2) (2017) 89.
[22] I. Astefanoaei, A. Stancu, Advanced thermo-mechanical analysis in the magnetic hyperthermia, J. Appl. Phys. 122 (16) (2017).
[23] R.E. Rosensweig, Heating magnetic fluid with alternating magnetic field, J. Magn. Magn. Mater. 252 (2002) 370–374.
[24] G. Singh, N. Kumar, P.K. Avti, Computational evaluation of effectiveness for intratumoral injection strategies in magnetic nanoparticle assisted thermotherapy, Int. J. Heat Mass Transfer 148 (2020) 119129.
[25] Y. Tang, T. Jin, R.C. Flesch, Y. Gao, M. He, Effect of nanofluid distribution on therapeutic effect considering transient bio-tissue temperature during magnetic hyperthermia, J. Magn. Magn. Mater. 517 (2021) 167391.
[26] J. Crank, The Mathematics of Diffusion, Oxford University Press, 1979.
[27] M. Salloum, R. Ma, D. Weeks, L. Zhu, Controlling nanoparticle delivery in magnetic nanoparticle hyperthermia for cancer treatment: experimental study in agarose gel, Int. J. Hyperth. 24 (4) (2008) 337–345.
[28] A.A. Golneshan, M. Lahonian, Diffusion of magnetic nanoparticles in a multi-site injection process within a biological tissue during magnetic fluid hyperthermia using lattice Boltzmann method, Mech. Res. Commun. 38 (6) (2011) 425–430.
[29] Y.-d. Tang, T. Jin, R.C. Flesch, Impact of different infusion rates on mass diffusion and treatment temperature field during magnetic hyperthermia, Int. J. Heat Mass Transfer 124 (2018) 639–645.
[30] A. Hervault, N.T.K. Thanh, Magnetic nanoparticle-based therapeutic agents for thermo-chemotherapy treatment of cancer, Nanoscale 6 (20) (2014) 11553–11573.
[31] H.H. Pennes, Analysis of tissue and arterial blood temperatures in the resting human forearm, J. Appl. Physiol. 1 (2) (1948) 93–122.
[32] M. Salloum, R. Ma, L. Zhu, Enhancement in treatment planning for magnetic nanoparticle hyperthermia: optimization of the heat absorption pattern, Int. J. Hyperth. 25 (4) (2009) 309–321.
[33] Y. Tang, H. Su, R.C. Flesch, T. Jin, An optimization method for magnetic hyperthermia considering nelder-mead algorithm, J. Magn. Magn. Mater. 545 (2022) 168730.
[34] P. Di Barba, F. Dughiero, E. Sieni, Synthesizing distributions of magnetic nanoparticles for clinical hyperthermia, IEEE Trans. Magn. 48 (2) (2012) 263–266.
[35] G. Venter, Review of optimization techniques, in books: Mechanical and mechatronic engineering, Wiley Online Library, 2010,
[36] Y.-D. Tang, T. Jin, R.C. Flesch, H.-Y. Jiang, Simultaneous optimization of injection dose and location for magnetic hyperthermia using metaheuristic algorithms, IEEE Trans. Magn. 56 (1) (2019) 1–6.
[37] P. Di Barba, F. Dughiero, E. Sieni, Field synthesis for the optimal treatment planning in Magnetic Fluid Hyperthermia, Arch. Electr. Eng. (2012) 57–67.
[38] Q. Jiang, F. Ren, C. Wang, Z. Wang, G. Kefayati, S. Kenjeres, K. Vafai, Y. Liu, H. Tang, On the magnetic nanoparticle injection strategy for hyperthermia treatment, Int. J. Mech. Sci. 235 (2022) 107707.
[39] B. Wu, Q. Jiang, Z. Wang, C. Wang, F. Ren, H. Tang, An optimization study considering MNP temporal evolution improves therapeutic efficacy in hyperthermia treatment, Int. J. Therm. Sci. 220 (2026) 110319.
[40] G.R. Fatigate, M. Lobosco, R.F. Reis, A 3D approach using a control algorithm to minimize the effects on the healthy tissue in the hyperthermia for cancer treatment, Entropy 25 (4) (2023) 684.
[41] C.L. Carter, C. Allen, D.E. Henson, Relation of tumor size, lymph node status, and survival in 24,740 breast cancer cases, Cancer 63 (1) (1989) 181–187.
[42] M. Singh, R. Ma, L. Zhu, Quantitative evaluation of effects of coupled temperature elevation, thermal damage, and enlarged porosity on nanoparticle migration in tumors during magnetic nanoparticle hyperthermia, Int. Commun. Heat Mass Transfer 126 (2021) 105393.
[43] J. Buongiorno, Convective transport in nanofluids, J. Heat Transf. (2006).
[44] B. Ghasemi, S. Aminossadati, A. Raisi, Magnetic field effect on natural convection in a nanofluid-filled square enclosure, Int. J. Therm. Sci. 50 (9) (2011) 1748–1756.
[45] L.S. Sundar, M.K. Singh, A.C. Sousa, Investigation of thermal conductivity and viscosity of Fe3O4 nanofluid for heat transfer applications, Int. Commun. Heat Mass Transfer 44 (2013) 7–14.
[46] J. Lang, B. Erdmann, M. Seebass, Impact of nonlinear heat transfer on temperature control in regional hyperthermia, IEEE Trans. Biomed. Eng. 46 (9) (1999) 1129–1138.
[47] E. Myrovali, N. Maniotis, A. Makridis, A. Terzopoulou, V. Ntomprougkidis, K. Simeonidis, D. Sakellari, O. Kalogirou, T. Samaras, R. Salikhov, et al., Arrangement at the nanoscale: Effect on magnetic particle hyperthermia, Sci. Rep. 6 (1) (2016) 37934.
[48] G. Bellizzi, O.M. Bucci, G. Chirico, Numerical assessment of a criterion for the optimal choice of the operative conditions in magnetic nanoparticle hyperthermia on a realistic model of the human head, Int. J. Hyperth. 32 (6) (2016) 688–703.
[49] E.A. Périgo, G. Hemery, O. Sandre, D. Ortega, E. Garaio, F. Plazaola, F.J. Teran, Fundamentals and advances in magnetic hyperthermia, Appl. Phys. Rev. 2 (4) (2015) 041302.
[50] E. Kosari, K. Vafai, Thermal tissue damage analysis for magnetothermal neuromodulation and lesion size minimization, Brain Multiphysics 1 (2020) 100014.
[51] Y.-d. Tang, R.C. Flesch, T. Jin, Injection strategy for the optimization of therapeutic temperature profile considering irregular tumors in magnetic hyperthermia, IEEE Trans. Magn. 54 (6) (2018) 1–6.
[52] O. Navarro-Hinojosa, S. Ruiz-Loza, M. Alencastre-Miranda, Physically based visual simulation of the Lattice Boltzmann method on the GPU: a survey, J. Supercomput. 74 (7) (2018) 3441–3467.
[53] J. Kennedy, R. Eberhart, Particle swarm optimization, in: Proceedings of ICNN'95-International Conference on Neural Networks, vol. 4, IEEE, 1995, pp. 1942–1948.
[54] Y. Tang, R.C. Flesch, T. Jin, Numerical investigation of temperature field in magnetic hyperthermia considering mass transfer and diffusion in interstitial tissue, J. Phys. D: Appl. Phys. 51 (3) (2017) 035401.
[55] U. Frisch, B. Hasslacher, Y. Pomeau, Lattice-gas automata for the Navier-Stokes equation, in: Lattice Gas Methods for Partial Differential Equations, CRC Press, 2019, pp. 11–18.
[56] Z. Guo, T. Zhao, A lattice Boltzmann model for convection heat transfer in porous media, Numer. Heat Transf. Part B 47 (2) (2005) 157–177.
[57] B. Wu, J. Lu, H. Lee, C. Shu, M. Wan, An explicit immersed boundary-reconstructed thermal lattice Boltzmann flux solver for thermal–fluid-structure interaction problems, Int. J. Mech. Sci. 235 (2022) 107704.
[58] H. Zhang, Lattice Boltzmann method for solving the bioheat equation, Phys. Med. Biol. 53 (3) (2008) N15.
[59] K. Das, S.C. Mishra, Estimation of tumor characteristics in a breast tissue with known skin surface temperature, J. Therm. Biol. 38 (6) (2013) 311–317.
[60] K. Das, R. Singh, S.C. Mishra, Numerical analysis for determination of the presence of a tumor and estimation of its size and location in a tissue, J. Therm. Biol. 38 (1) (2013) 32–40.
[61] D. d'Humières, Multiple–relaxation–time lattice Boltzmann models in three dimensions, Philos. Trans. R. Soc. Lond. Ser. A Math. Phys. Eng. Sci. 360 (1792) (2002) 437–451.
[62] P. Lallemand, L.-S. Luo, Theory of the lattice Boltzmann method: Dispersion, dissipation, isotropy, Galilean invariance, and stability, Phys. Rev. E 61 (6) (2000) 6546.
[63] S. Girimaji, Lattice Boltzmann method: Fundamentals and engineering applications with computer codes, 2013.
[64] Q. Liu, X.-B. Feng, Y.-L. He, C.-W. Lu, Q.-H. Gu, Three-dimensional multiple-relaxation-time lattice Boltzmann models for single-phase and solid-liquid phase-change heat transfer in porous media at the REV scale, Appl. Therm. Eng. 152 (2019) 319–337.
[65] L. Li, R. Mei, J.F. Klausner, Boundary conditions for thermal lattice Boltzmann equation method, J. Comput. Phys. 237 (2013) 366–395.
[66] H. Yoshida, M. Nagaoka, Multiple-relaxation-time lattice Boltzmann model for the convection and anisotropic diffusion equation, J. Comput. Phys. 229 (20) (2010) 7774–7795.
[67] P. Moroz, S.K. Jones, J. Winter, B.N. Gray, Targeting liver tumors with hyperthermia: ferromagnetic embolization in a rabbit liver tumor model, J. Surg. Oncol. 78 (1) (2001) 22–29.
[68] Y. Shi, R.C. Eberhart, Empirical study of particle swarm optimization, in: Proceedings of the 1999 Congress on Evolutionary Computation-CEC99 (Cat. No. 99TH8406), vol. 3, IEEE, 1999, pp. 1945–1950.
[69] J.J. Liang, A.K. Qin, P.N. Suganthan, S. Baskar, Comprehensive learning particle swarm optimizer for global optimization of multimodal functions, IEEE Trans. Evol. Comput. 10 (3) (2006) 281–295.
[70] G. He, N.-j. Huang, A modified particle swarm optimization algorithm with applications, Appl. Math. Comput. 219 (3) (2012) 1053–1060.
[71] Y. Wang, W. Zhao, G. Zhou, C. Wang, Analysis and parametric optimization of a novel sandwich panel with double-V auxetic structure core under air blast loading, Int. J. Mech. Sci. 142 (2018) 245–254.

[72] J. Xu, Y. Chen, Y. Tai, X. Xu, G. Shi, N. Chen, Vibration analysis of complex fractional viscoelastic beam structures by the wave method, Int. J. Mech. Sci. 167 (2020) 105204.
[73] C. Ye, J. Yang, H. Zhao, H. Ding, Task-dependent workpiece placement optimization for minimizing contour errors induced by the low posture-dependent stiffness of robotic milling, Int. J. Mech. Sci. 205 (2021) 106601.
[74] X. Ding, Z. Tong, Y. Liu, S. Liu, Dynamic axial crush analysis and design optimization of a square multi-cell thin-walled tube with lateral variable thickness, Int. J. Mech. Sci. 140 (2018) 13–26.
[75] Y. Shi, R. Eberhart, A modified particle swarm optimizer, in: 1998 IEEE International Conference on Evolutionary Computation Proceedings. IEEE World Congress on Computational Intelligence (Cat. No. 98TH8360), IEEE, 1998, pp. 69–73.
[76] Z.-H. Zhan, J. Zhang, Y. Li, H.S.-H. Chung, Adaptive particle swarm optimization, IEEE Trans. Syst. Man Cybern. B 39 (6) (2009) 1362–1381.